CHALMERS
UNIVERSITY OF TECHNOLOGY

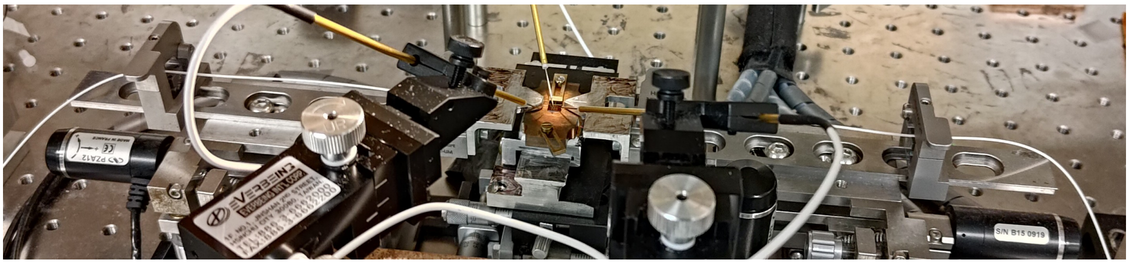

# Design of a microcomb based optical oscillator with a low RF repetition rate phase noise

Master's thesis in Wireless Photonics and Space Engineering


ASHISH KRISHNA MURTHY ADIGA

DEPARTMENT OF ELECTRICAL ENGINEERING

CHALMERS UNIVERSITY OF TECHNOLOGY
Gothenburg, Sweden 2026
www.chalmers.se

Master's thesis 2026

# Design of a microcomb based optical oscillator with a low RF repetition rate phase noise

ASHISH KRISHNA MURTHY ADIGA

Department of Electrical Engineering
*Division of Microtechnology and Nanoscience (MC2)*
Photonics Laboratory
Chalmers University of Technology
Gothenburg, Sweden 2026

Design of a microcomb based optical oscillator with a low RF repetition rate phase noise
ASHISH KRISHNA MURTHY ADIGA



Ericsson Supervisors: Mikael Hörberg, Johan Karlsson, Ericsson
Chalmers Supervisor: Yvan Klaver, MC2
Examiner: Victor Torres Company, MC2

Master's Thesis 2026
Department of Electrical Engineering
Division of Microtechnology and Nanoscience (MC2)
Photonics Laboratory
Chalmers University of Technology
SE-412 96 Gothenburg
Telephone +46 31 772 1000

Cover: Optical bench setup of the optical oscillator.

Typeset in LaTeX
Printed by Chalmers digitaltryck
Gothenburg, Sweden 2026

Design of a microcomb based optical oscillator with a low RF repetition rate phase noise
ASHISH KRISHNA MURTHY ADIGA
Department of Electrical Engineering
Chalmers University of Technology

# Abstract

Advanced wireless communication systems operating at E-band frequencies (60–90 GHz) and beyond require oscillators with extremely low phase noise, a demand that is increasingly difficult to meet with conventional electronic approaches. Photonic signal generation via two-point optical frequency division(OFD) addresses this challenge by transferring the inherent frequency stability of optical resonators to the microwave domain. Silicon nitride ($Si_3N_4$) microresonator frequency combs, in particular the photonic molecule architecture, comprising two evanescently coupled microrings, offer a chip-scale route to integrated, low phase noise local oscillators suitable for next-generation communication links.

This thesis presents the design, implementation, and experimental characterization of a $Si_3N_4$ photonic molecule microcomb operated as an RF oscillator through two-point OFD. Multiple dissipative Kerr soliton (DKS) states were accessed and characterized using a single pump laser. Two-point optical stabilization via optical injection locking (OIL) of an auxiliary laser was investigated across all accessible soliton numbers. The repetition rate at ≈49.921 GHz was characterized using a high-speed photodiode and a Rohde & Schwarz phase noise analyzer, with additional measurements at 12.48 GHz using a ÷4 RF divider.

Contrary to the original intent, OIL with the auxiliary laser consistently degraded the repetition-rate phase noise relative to the free-running configuration. Two unexpected results were observed. First, higher-order soliton states (two-soliton and above) exhibited lower phase noise than the single-soliton state, attributed to increased carrier power and a stabilizing role of the avoided mode crossing (AMX). Second, the measured phase noise fell marginally below the theoretical two-point OFD limit, interpreted as evidence of passive pump-noise filtering by the coupled resonator. A preliminary system-level evaluation on an Ericsson 5G testbed yielded a signal to noise and interference ratio (SNIR) of 26 dB, demonstrating a feasible but not yet communication-grade photonic local oscillator. These results motivate further study of coupled-resonator geometries as passive noise-suppression mechanisms for integrated microwave photonic sources.

Keywords: microcomb, photonic molecule, coupled microring resonator, phase noise, optical frequency division, repetition rate, soliton, microwave photonics, optical injection locking.

# Acknowledgements

I would like to express my sincere gratitude to the people who supported and guided me throughout the course of this master's thesis.
First and foremost, I would like to thank Professor Victor Torres Company, the examiner of this thesis, for introducing me to the field of Photonics and Lasers and for providing the opportunity to carry out this work within an academically stimulating environment. His insights and perspective helped shape the overall direction of the project.
I am especially grateful to my Chalmers supervisor, Yvan Klaver, for his continuous guidance and technical support during the laboratory work carried out at the Photonics Laboratory at Chalmers. His practical advice, critical feedback, and availability for discussion were invaluable throughout the experimental phases of the project.
I would also like to thank my Ericsson supervisors, Mikael Hörberg and Johan Karlsson, for their support from an industrial perspective. Their guidance helped ensure that the work remained relevant to real-world communication systems and aligned with the objectives of the Ericsson radio testbed.
I would like to extend my sincere appreciation to David Hiselius, my fellow master's thesis collaborator, whose contribution to the RF aspects of this work was immense. While this thesis primarily focused on the optical components and investigations, David carried out the RF-related work with great expertise and dedication. His efforts, technical knowledge, and close collaboration were essential to the successful realization and completion of this project.
I would like to acknowledge my manager at Ericsson, Martin Myhr and Ericsson for providing the opportunity and framework for this master's thesis, as well as access to the industrial testbed used for system-level evaluation.
I would also like to thank the Fiber Lab and Microwave Electronics Lab at Chalmers for providing access to the Signal Source Analyzers necessary for this work.
My sincere thanks also go to everyone at the Photonics Laboratory at Chalmers for creating a welcoming and collaborative research environment.
Finally, I would like to thank my family in India for their constant encouragement and support throughout my two-year master's program in Sweden. Their support has been essential to completing this journey.

ASHISH KRISHNA MURTHY ADIGA, Gothenburg, May 2026

# List of Acronyms

| | |
|---|---|
| AMX | Avoided Mode Crossing |
| ASE | Amplified Spontaneous Emission |
| CEO | Carrier-Envelope Offset |
| COSH | Coherent Optical Self-Heterodyne |
| DANL | Displayed Average Noise Level |
| DKS | Dissipative Kerr Soliton |
| EDFA | Erbium-Doped Fibre Amplifier |
| ESA | Electrical Spectrum Analyser |
| FBG | Fibre Bragg Grating |
| FSR | Free Spectral Range |
| GH | Gordon–Haus |
| GVD | Group-Velocity Dispersion |
| LLE | Lugiato–Lefever Equation |
| LNA | Low Noise Amplifier |
| LO | Local Oscillator |
| MI | Modulation Instability |
| MIMO | Multiple Input Multiple Output |
| NTC | Negative Temperature Coefficient |
| OFC | Optical Frequency Comb |
| OFD | Optical Frequency Division |
| OI | Optical Injection |
| OIL | Optical Injection Locking |
| OPM | Optical Power Meter |
| OSA | Optical Spectrum Analyser |
| PC | Polarisation Controller |
| PD | Photodiode |
| PID | Proportional-Integral-Derivative |
| PLL | Phase-Locked Loop |
| PNA | Phase Noise Analyser |
| PSD | Power Spectral Density |
| RF | Radio Frequency |
| SNIR | Signal-to-Noise-and-Interference Ratio |
| SSB | Single-Sideband |
| TRN | Thermorefractive Noise |
| VOA | Variable Optical Attenuator |
| WDM | Wavelength Division Multiplexing |
| XPIC | Cross Polarisation Interference Cancellation |

# Contents

# List of Figures

# List of Tables

# 1
# Introduction

Scaling wireless links toward E-band frequencies (60-90 GHz) and beyond requires the phase noise of the local oscillator(LO) to be low because because frequency multiplication, wide bandwidths, high-order modulation, OFDM sensitivity, and coherent beamforming all make the system increasingly dependent on a spectrally pure LO. At these frequencies, transistor flicker noise increases with carrier frequency, while even high-performance dielectric microwave cavity resonators, such as sapphire-based structures, remain limited by material loss and fabrication imperfections, with typical loaded quality factors in the range of $10^4$ to $8*10^5$ [3]. Advanced link technologies—such as high-order modulation schemes (e.g., 1024-QAM) [4], cross-polarisation interference cancellation (XPIC) [5], and Multiple-Input Multiple-Output (MIMO) spatial multiplexing [6] require an LO source with a low phase noise. The phase noise of conventional electronic LO sources is emerging as a key factor limiting the performance of the aforementioned link technologies.

Photonic signal generation offers a fundamentally different starting point compared to electronic signal generation. Optical resonators achieve quality factors of $10^6$ to $10^8$, dwarfing those of microwave resonators by several orders of magnitude [7]. The technique of 2-point optical frequency division (OFD) allows this optical stability to be transferred to the microwave domain: the RF output phase noise is suppressed relative to the optical reference by the square of the optical-to-microwave frequency ratio. Demonstrations of 2-point OFD-based signal generation have already exceeded the phase-noise performance of the best electronic oscillators [8], establishing this approach as a credible route to ultra-low-noise RF sources.

Performing 2-point OFD requires an optical frequency comb (OFC), that is a coherent grid of equally spaced optical frequencies. A microresonator frequency comb generates such an OFC by driving a high-$Q$ $Si_3N_4$ microresonator with a CW pump laser [9]. Detecting an OFC on a fast photodiode produces a microwave signal at the comb repetition rate [10, 11]. Since their first demonstration in the mid-2000s [9], microresonator combs have found application in optical atomic clocks [12], coherent WDM communications [13], and low-noise microwave synthesis [14].

However, frequency combs generated in a single microring resonator require the pump to be held far from the cavity resonance, so most incident pump power is not coupled and never converted into comb light. This means low comb-line power at the photodetector and a correspondingly weak RF carrier [1].

The photonic molecule, a main ring evanescently coupled to a secondary auxiliary ring, circumvents this constraint by shifting the pump coupling condition, allowing more pump power to be converted to comb lines [1]. The result is stronger comb-line power and a stronger RF beat at the photodetector.

This thesis reports repetition-rate phase noise measurements of a $Si_3N_4$ photonic molecule microcomb operated as an RF oscillator. The project was conceived as a two-point OFD demonstration, with a pump laser and an auxiliary reference laser providing optical injection locking (OIL). Pump-only soliton generation was achieved reproducibly across multiple soliton numbers. Contrary to our expectations, when the auxiliary laser was introduced, the repetition-rate phase noise deteriorated in every measurement. Higher-order soliton states exhibited systematically lower phase noise than the single-soliton state. This was accompanied by one additional unexpected observation: the best measured traces fell marginally below the theoretical 2-point OFD limit (defined as the pump-laser phase noise scaled by the targeted ≈34 dB optical-to-RF division factor). Understanding and documenting these findings forms the core of this thesis.

## Objectives

The primary objective of this project is to determine whether an OFC generated using a coupled-microring resonator can serve as a low-phase-noise microwave source through 2-point optical frequency division (OFD), and to identify the physical mechanisms that ultimately limit its performance.
The work is therefore guided by the following research questions:

1. To what extent do the intrinsic frequency-noise and phase-noise properties of the available CW pump lasers determine the achievable repetition-rate phase noise after optical frequency division?
2. Can N-soliton states have a lower repetition rate phase noise than a single soliton state?
3. Does auxiliary laser injection improve or degrade the microwave phase-noise performance of the soliton states, and what physical mechanisms govern this behaviour?
4. Does the experimentally observed repetition-rate phase noise of soliton combs without optical injection locking an auxiliary laser, perform better than a soliton comb with optical injection locking an auxiliary laser?

The remainder of this report is structured as follows. Chapter 2 covers the theoretical background, including dissipative Kerr solitons, the 2-point OFD phase noise suppression mechanism, two-point optical stabilisation, and measurement considerations at millimetre-wave frequencies. Chapter 3 describes the experimental methods. Chapter 4 presents and discusses the results. Chapter 5 draws conclusions and outlines future work.

# 2

# Theory

This chapter provides the essential theoretical background needed to understand the operating principles, design choices, and experimental observations presented in this thesis. It explains the physical mechanisms underlying the generation and stabilization of dissipative Kerr soliton (DKS) states in a silicon nitride photonic molecule microresonator, the transfer of optical stability to the microwave domain via 2-point optical frequency division (OFD), and the key noise processes that determine the repetition-rate phase noise of the resulting RF oscillator.

Section 2.1 introduces Kerr microresonator frequency combs, progressing from basic microring resonator physics through nonlinear cavity dynamics to the formation and properties of DKS states. Section 2.2 describes the photonic molecule (coupled-microring) architecture and its advantages for power-efficient comb generation. Sections 2.3 and 2.4 cover frequency/phase noise concepts and the 2-point OFD mechanism that links optical resonator stability to microwave performance. Finally, Sections 2.5 and 2.6 address optical injection locking and photodetection considerations, which are directly relevant to the stabilization approach and measurement techniques used in this work.

This foundation is necessary to interpret the experimental results-particularly the soliton-number dependence of phase noise, the effect of optical injection, and evidence of passive noise filtering, reported in Chapter 4.

## 2.1 Kerr microresonator frequency combs

A microresonator frequency comb is generated when a CW pump laser couples into a high-$Q$ microresonator experiencing a sufficiently strong Kerr nonlinearity, resulting in the conversion of pump light into a coherent, equally spaced grid of optical frequencies. The subsections below build up this picture step by step: the ring resonator and its resonances, the comb frequency equation and repetition rate, the nonlinear dynamics governing comb formation, and finally the dissipative Kerr soliton, the coherent pulsed state exploited in this work.

### 2.1.1 Microring resonator basics

A microring resonator consists of a waveguide loop evanescently coupled to a bus waveguide through a narrow gap, as illustrated schematically in Fig. 2.1. Light circulating in the ring builds up when the round-trip phase is a multiple of $2\pi$ (resonance condition), and leaks back into the bus waveguide otherwise. The resonator quality factor $Q$ denotes the ratio of stored electromagnetic energy to the power dissipated per oscillation cycle; equivalently, it governs how many optical cycles elapse before the intracavity energy decays to $e^{-1}$ of its initial value [1, 11]. High $Q$ is important for two reasons: it increases intracavity power for a given input pump power, and it lowers the threshold for parametric oscillation (Section 2.1.3.3). In $Si_3N_4$ rings, sidewall roughness from the dry-etch step dominates propagation loss; waveguide geometry optimization during fabrication is therefore the main lever for achieving the high-$Q$ values required for efficient comb generation [15, 1].

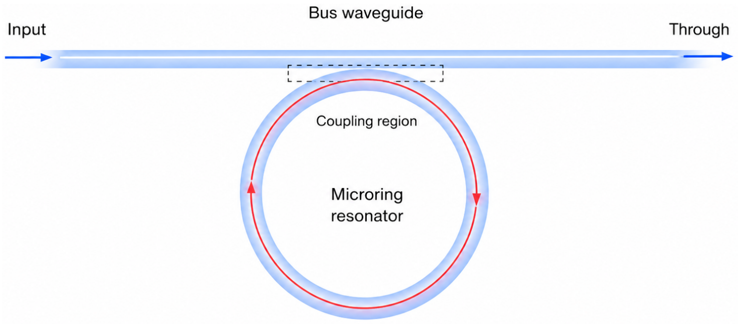


**Figure 2.1:** A single microring resonator schematic.

### 2.1.2 Comb frequency equation and repetition rate

A microring of circumference $L$ supports a series of resonances separated in frequency by the free spectral range (FSR). To leading order,

$$f_{\text{rep}} \approx \frac{c}{n_g L}, \tag{2.1}$$

where $c$ is the vacuum speed of light and $n_g$ is the waveguide group refractive index. When a frequency comb is generated, the comb teeth are equally spaced by $f_{\text{rep}}$. Labelling each tooth by an integer mode index $n$ measured from the pump, its absolute optical frequency is

$$\nu_n \;=\; f_{\text{CEO}} + n\, f_{\text{rep}}, \tag{2.2}$$

where $f_{\text{CEO}}$ is the carrier-envelope offset frequency, which reflects the accumulated difference between phase and group velocities over one round trip [16, 1]. Complete frequency stabilization of the comb grid requires independent control of both $f_{\text{rep}}$ and $f_{\text{CEO}}$; the two-point stabilization scheme designed to achieve this is described in Section 2.4.

### 2.1.3 Nonlinear cavity dynamics and the lugiato-lefever equation

The joint action of cavity loss, coherent pump driving, group-velocity dispersion (GVD), and Kerr self-phase modulation (SPM) on the intracavity field envelope $A$

is captured by the Lugiato–Lefever equation (LLE), first derived for spatial patterns in passive optical cavities [17] and later extended to Kerr-comb generation in microresonators [18, 1]. The LLE is given as:

$$\frac{\partial A}{\partial \tau} = \frac{1}{t_R}\left[\left(-\sigma - i\delta_0 - \frac{iL\beta_2}{2}\frac{\partial^2}{\partial t^2} + iL\gamma|A|^2\right)A + i\sqrt{\theta}\,A_{\text{in}}\right], \tag{2.3}$$

where $\tau$ is a slow time variable advancing by one unit per round trip, $t_R$ is the round-trip period, $\sigma = (\theta + \alpha L)/2$ combines the coupler transmission $\theta$ with the round-trip loss $\alpha L$, $\delta_0$ is the pump-to-resonance detuning, $\beta_2$ is the GVD coefficient, $\gamma$ is the Kerr coefficient, and $A_{\text{in}}$ is the input pump field. The LLE links all four physical effects i.e. loss, pump drive, dispersion ($\beta_2$ term), and Kerr SPM ($iL\gamma|A|^2$ term) in a single dynamical equation.

#### 2.1.3.1 Kerr optical bistability

The Kerr SPM term couples intracavity power to the effective refractive index. As the pump frequency is swept from the blue side toward a resonance, the growing intracavity field shifts the resonance toward the red through SPM, until the system collapses abruptly onto the low-power branch of the resulting bistability curve. For a single ring resonator, access to the dissipative Kerr soliton (DKS) regime becomes possible once the system reaches the effectively red-detuned upper branch of the bistability curve [19] shown in the orange trace in Fig. 2.2. In coupled ring resonator, it is possible to achieve a single soliton while remaining on the blue detuned region of the shifted resonance.

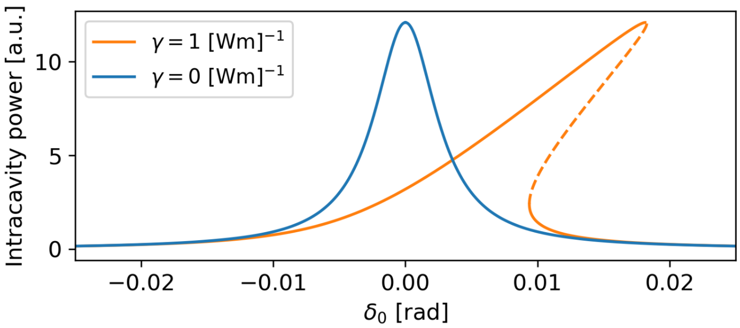


**Figure 2.2:** An illustrative bistability response showing the variation of intracavity power together with the Kerr-induced resonance displacement, where the nonlinear interaction strength is characterized by the coefficient $\gamma$ (adapted from [1]).

#### 2.1.3.2 Thermal bistability

In $Si_3N_4$, partial optical absorption also heats the waveguide, generating a thermally driven resonance shift on a millisecond timescale. This thermally induced bistability acts separately from the Kerr bistability described above: as the pump approaches the resonance from the blue, absorbed power heats the waveguide and shifts the resonance further red, which can further increase intracavity power and trigger a runaway thermal shift. Careful control of the pump scan rate is therefore necessary to navigate both bistabilities reproducibly and reach stable soliton states [19].

#### 2.1.3.3 Modulation instability

In the anomalous-dispersion regime ($\beta_2 < 0$), vacuum-noise sidebands at offset frequencies $\pm\Delta\Omega_m$ from the pump experience parametric gain once the circulating power surpasses the threshold [1]

$$P_{\text{th}} = \frac{\sigma}{\gamma L}. \tag{2.4}$$

Because $\sigma \propto 1/Q$, a higher quality factor directly lowers the pump power required to initiate comb formation [11, 18]. Also the intracavity circulating power scales with $Q$, so the threshold pump power in the bus waveguide scales as $1/Q^2$, making $Q$ a critical design parameter. Equation (2.4) provides an estimate for the threshold of modulational instability, corresponding to the initial growth of parametric sidebands from vacuum fluctuations. This threshold sets a lower bound for modulation instability initiation and the soliton states are generated when the pump laser power is 10 dBm above this lower bound. The photonic molecule chip used in this work has a loaded Q of the order of $10^6$.

### 2.1.4 Dissipative kerr solitons

When the pump red-detuning is sufficiently large, the intracavity field settles into a *dissipative Kerr soliton* (DKS): a stable, self-reinforcing circulating pulse satisfying two balance conditions [19]. The *first balance condition* is in the temporal domain: Kerr SPM offsets the dispersive pulse broadening that GVD would otherwise impose. The *second balance condition* is in the energy domain: parametric gain from the CW pump background exactly compensates the round-trip cavity loss.

A single circulating soliton produces an optical spectrum with a $\text{sech}^2$ envelope. The additional wavelength-dependent modulation of the comb-line amplitudes is attributed to spectral filtering arising from the coupled auxiliary resonator, which can introduce wavelength-dependent mode hybridization and interference effects (Fig. 2.3).

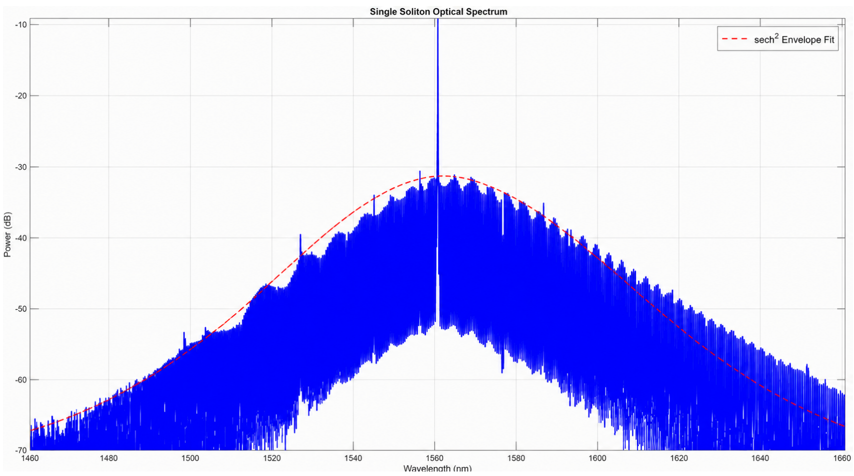


**Figure 2.3:** Optical Spectrum of the single soliton state generated using a coupled microring resonator. The $\text{sech}^2$ envelope was fitted directly to the measured OSA spectrum in the wavelength domain using the dB-scaled power trace.

In multi-soliton states, where two or more solitons co-propagate, interference between the individual $\text{sech}^2$ pulses produces a periodic modulation of the envelope. The spatial frequency of this modulation reflects the angular separation between the solitons within the ring. [1]. Multi-soliton states are central to the results of this thesis. Examples of optical spectra for two and three-soliton states are shown in the Figures 2.4, 2.5.

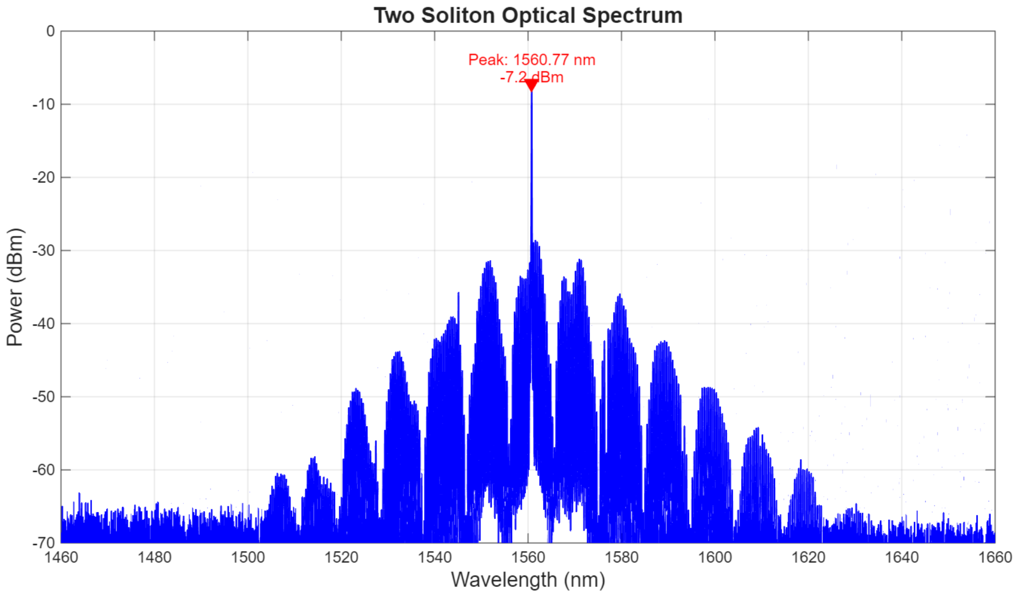


**Figure 2.4:** Optical Spectrum of the two soliton state generated using a coupled microring resonator.

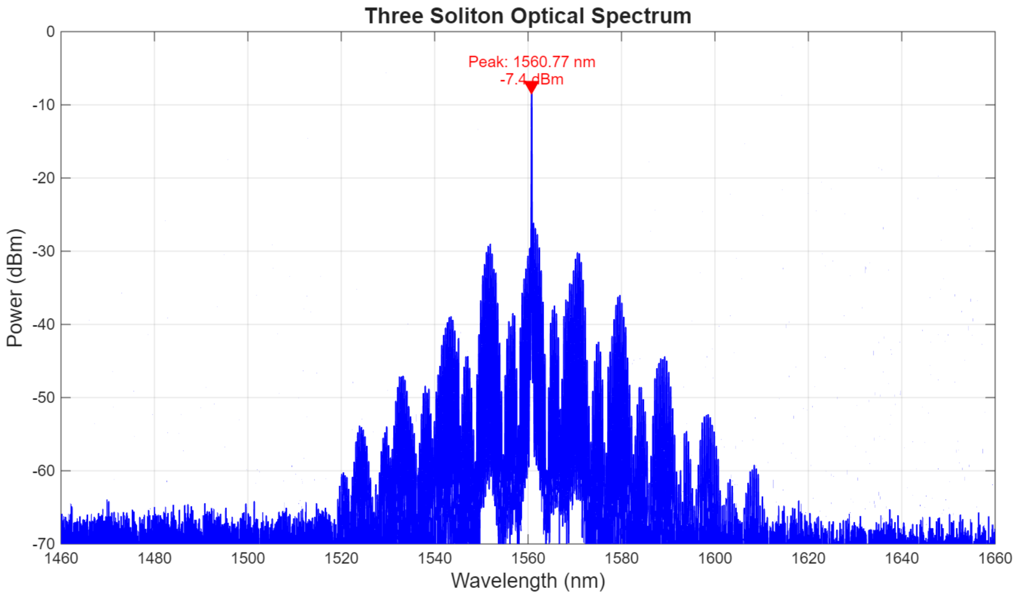


**Figure 2.5:** Optical Spectrum of the three soliton state generated using a coupled microring resonator.

A prominent residual pump line in the optical spectrum is fully compatible with

dissipative Kerr soliton operation in micro-resonators and arises from the continuous-wave driving field required to sustain the intracavity soliton state. Consequently, the optical spectrum generally consists of both the soliton envelope and a coherent CW background.
Experimentally, DKS operation is reached by scanning the pump from the blue side toward the red side of a resonance (see Chapter 3). Accessing a specific soliton number reproducibly additionally requires matching the pump scan rate to the thermal state of the resonator at the moment of the transition [19].

## 2.2 Photonic molecules and coupled microring resonators

This section explains the coupled-ring architecture used in this work. The architecture consists of a secondary (auxiliary) ring resonator that is evanescently coupled to the main ring resonator, as shown in Fig. 2.6. In addition, an Ω-shaped gold heater ring is deposited above the auxiliary ring separated by a silica barrier layer to enable thermo-optic tuning.

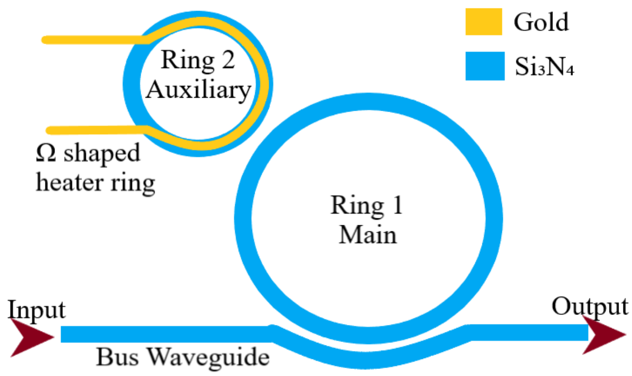


**Figure 2.6:** Coupled microring Resonator(Photonic Molecule) Schematic.

The power-efficiency motivation is given first, followed by the supermode physics, the avoided mode crossing, and the resulting intracavity power distribution.

### 2.2.1 Conversion efficiency and the motivation for coupled rings

DKS combs generated in a single microring face a fundamental power-efficiency limit: stable soliton operation requires the pump to be held well to the red of the cavity resonance, so a large fraction of the incident pump power is rejected at the bus-ring coupler and never converts into comb light[1].
Adding a secondary ring evanescently coupled to the main resonator provides an architecture that moves past this ceiling. The shift of the supermode for the pumped mode (described in the next subsection) allows a greater fraction of pump power

to be coupled to the comb lines. The practical pay-off is stronger per-tooth comb power and a stronger RF beat at the photodetector, a decisive advantage for any optical RF-oscillator application where the detected RF carrier power determines the measurement noise floor (see Section 2.6).

### 2.2.2 Supermode formation and heater tunability

The chip characterized in this work contains two $Si_3N_4$ microrings of intentionally different circumferences, each equipped with an integrated resistive heater. Applying power to a heater shifts the refractive index of that ring via the thermo-optic effect, thereby shifting its resonance frequencies. Evanescent coupling through the gap between the rings causes pairs of modes that approach each other in frequency to hybridize into symmetric and anti-symmetric supermodes [20, 1].
The supermode eigenfrequencies are [1]:

$$\omega_{\pm} = \frac{\omega^{(1)} + \omega^{(2)}}{2} \pm \sqrt{\left(\frac{\omega^{(1)} - \omega^{(2)}}{2}\right)^2 + \kappa^2}, \tag{2.5}$$

where $\omega^{(1)}$ and $\omega^{(2)}$ are the bare resonance frequencies of the isolated main and auxiliary rings, and $\kappa$ is the inter-ring coupling rate. Hybridization is strongest when the two bare resonances are nearly degenerate ($|\omega^{(1)} - \omega^{(2)}| \lesssim \kappa$), and adjusting the auxiliary ring heater voltage continuously tunes the hybridization. Figure 2.7 shows the laser frequency scan response observed as the auxiliary resonance is shifted across the primary resonance through an increase in the auxiliary heater voltage.
At the wavelength where two uncoupled resonances would coincide, inter-ring coupling causes the frequencies to repel rather than cross, resulting in an avoided mode crossing (AMX). Equation (2.5) gives this directly: the two supermode frequencies $\omega_{\pm}$ maintain a minimum splitting of $2\kappa$ even when $\omega^{(1)} = \omega^{(2)}$. In the through port transmission spectrum, this manifests as a characteristic double-dip feature. Such an AMX has limited tunability and thus operating wavelength. In the device used in this work, an AMX was located at 1560.9 nm, so it was set as the pump operating wavelength.

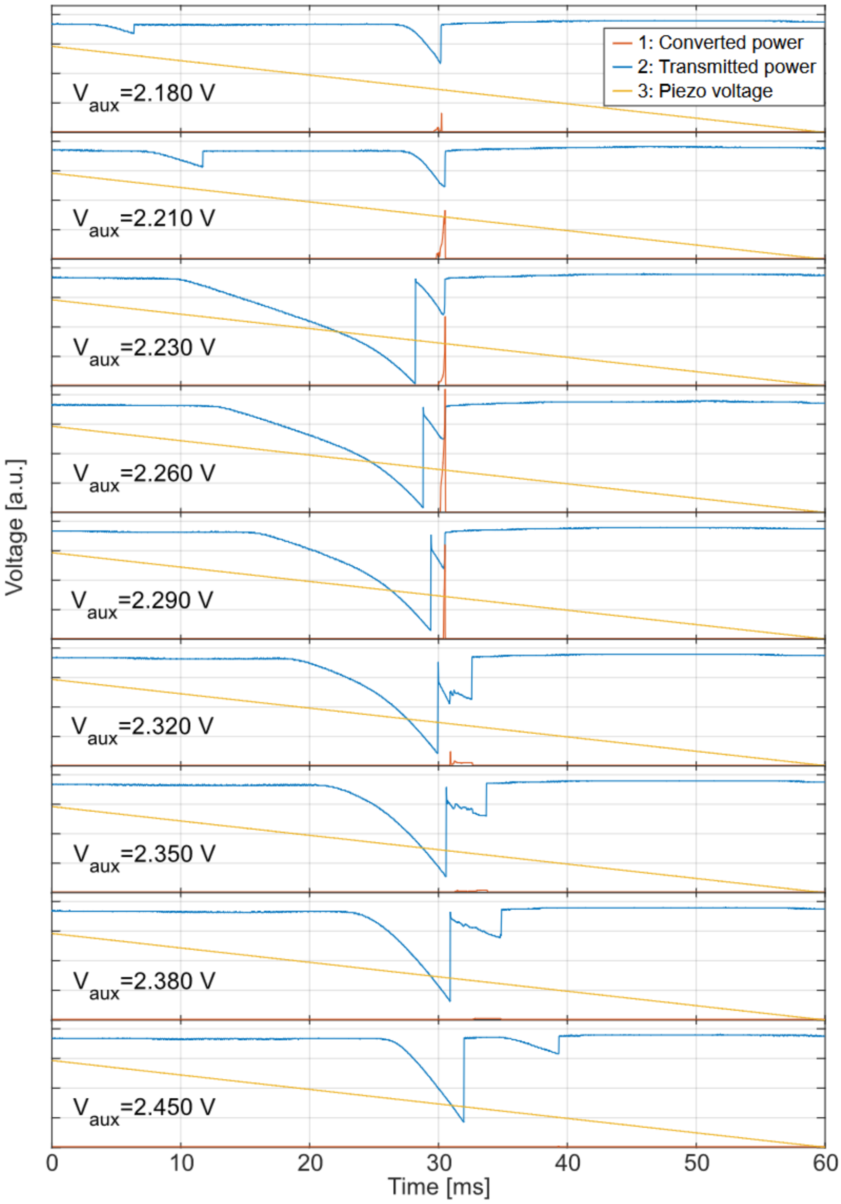


**Figure 2.7:** In the above figure, the wavelength of the continuous-wave (CW) laser is tuned by applying a ramp signal to a piezoelectric actuator located within the laser cavity. An auxiliary voltage, $V_{\mathrm{aux}}$, is supplied to the secondary ring's heater. The output shown represents the oscilloscope trace obtained while the piezo voltage is decreased linearly, corresponding approximately to a linear frequency sweep from the blue-detuned region toward the red-detuned region. In this configuration, the scan rate is about 0.2 GHz/ms. Both the transmitted optical power and the converted power are directly proportional to the recorded voltage. The laser frequency scan response is observed as the auxiliary resonance is shifted across the primary resonance through an increase in the auxiliary heater voltage. During this process, the laser frequency decreases by nearly 2 GHz over a time interval of 10 ms. Reproduced from [1].

### 2.2.3 Intracavity power distribution and DKS formation

The coupled-ring geometry controls how circulating optical power is distributed between the two rings. When the pump drives the lower-frequency (symmetric) supermode and the uncoupled auxiliary resonance is at a slightly higher frequency than the main ring resonance, the symmetric supermode has greater amplitude in the main ring. Higher CW background power in the main ring is thus a requirement, and coupled-LLE modeling by Helgason [1] confirms that DKS formation preferentially occurs in the ring sustaining the stronger background field, as that ring reaches the parametric oscillation threshold first.

Keeping the uncoupled auxiliary resonance at a lower frequency than the main ring resonance inverts this power distribution, leading to DKS formation primarily in the auxiliary ring. This sensitivity made auxiliary ring heater optimization a non-trivial experimental task (see Chapter 3): only a narrow heater-voltage range simultaneously achieved the desired power distribution and supported stable DKS formation in the main ring.

## 2.3 Frequency noise and phase noise

Phase noise $\mathcal{L}(f)$, expressed in dBc/Hz, quantifies the spectral purity of an oscillator by comparing the noise power in a 1 Hz bandwidth centered at Fourier offset $f$ from the carrier with the total carrier power. Its relationship to the one-sided phase noise power spectral density (PSD) $S_\phi(f)$ (units: rad$^2$/Hz) is [21]

$$\mathcal{L}(f) = 10\log_{10}\left(\frac{1}{2}S_\phi(f)\right). \tag{2.6}$$

Although $S_\phi(f)$ is defined as a one-sided phase-noise PSD, $\mathcal{L}(f)$ is defined as the noise power in a *single* sideband relative to the carrier. For small phase fluctuations, the phase-noise power is shared equally between the upper and lower sidebands, giving

$$\mathcal{L}_{\mathrm{lin}}(f) = \frac{S_\phi(f)}{2} \tag{2.7}$$

in linear units. Hence, the factor of 1/2 arises from the single-sideband definition of $\mathcal{L}(f)$ and not from a conversion between one-sided and two-sided PSDs.

An equally informative representation is the frequency noise PSD $S_\nu(f)$ (units: Hz$^2$/Hz), [21]:

$$S_\nu(f) = f^2 \cdot S_\phi(f) = 2 \cdot f^2 \cdot 10^{\mathcal{L}(f)/10}. \tag{2.8}$$

### 2.3.1 Phase noise mechanisms and spectral slopes

Oscillator phase noise spectra are not spectrally flat; they display distinct power-law segments, each traceable to a specific physical noise process. The standard decomposition [21] writes

$$S_\phi(f) = \sum_i \frac{h_i}{f^i}, \tag{2.9}$$

with each term interpretable as follows. An $f^{-3}$ slope in phase noise (equivalently $f^{-1}$ in frequency noise) is the signature of *flicker frequency noise*, arising from $1/f$ fluctuations in the instantaneous frequency and characteristic of low-offset behavior in semiconductor laser sources. An $f^{-2}$ phase noise slope (flat frequency noise) reflects *white frequency noise*, which dominates the mid-offset range in free-running soliton oscillators driven by a pump with a Lorentzian lineshape. A flat $f^0$ plateau at large offsets corresponds to *white phase noise*, arising from shot noise at the photodetector or thermal noise in the measurement instrument.
In the microcomb system studied here, pump-laser fluctuations are the dominant noise source, which gets imprinted onto the comb repetition rate. The Toptica CTL external-cavity diode lasers employed as pump and auxiliary sources exhibit a predominantly $f^{-2}$ phase noise slope above the stabilization bandwidth of their internal frequency-locking loop, which combined with the 2-point OFD suppression in Eq. (2.11) predicts an $f^{-2}$ slope in the repetition-rate phase noise.

### 2.3.2 Thermorefractive noise and Gordon–Haus jitter

Two intrinsic noise processes set a fundamental lower bound on repetition-rate phase noise that is independent of pump laser quality.
**Thermorefractive noise (TRN)** originates in spontaneous thermodynamic temperature fluctuations in the resonator waveguide core. These fluctuations perturb the local refractive index through the thermo-optic coefficient, modulating the effective optical path length and the cavity resonance frequency. The resulting frequency noise PSD for a $Si_3N_4$ ring of volume $V$ at temperature $T$ is [22, 23, 24]

$$S_\nu^{\mathrm{TRN}}(f) = \frac{k_B T^2}{\rho c_p V}\left(\frac{\partial n}{\partial T}\right)^2 \frac{\nu_0^2}{n^2} \cdot \frac{\tau_D}{(\pi f \tau_D)^2 + 1}, \tag{2.10}$$

where $\rho$ is the mass density, $c_p$ the specific heat, $\partial n/\partial T \approx 2.5 \times 10^{-5}\,\mathrm{K}^{-1}$ the $Si_3N_4$ thermo-optic coefficient, and $\tau_D$ the thermal diffusion time, which is set by heat flow through the oxide cladding and substrate [24]. The estimated TRN spectrum is plotted in Fig. 2.8.
**Gordon–Haus (GH) jitter** was first described for fibre-optic soliton transmission [25], where random amplified spontaneous emission events perturb the soliton centre frequency and cause a cumulative timing random walk. An equivalent process operates in microresonator solitons [26]: vacuum fluctuations coupled into the cavity through the bus-waveguide coupling port—the microresonator analogue of amplified spontaneous emission in fibre systems—produce stochastic photon-number fluctuations that perturb the soliton peak power, shift the effective nonlinear resonance, and generate a phase random walk in the repetition rate.
The GH contribution was estimated using [27]:

$$S_{\mathrm{f_{rep}}}^{GH}(f) \approx \frac{\hbar\omega_0}{E_s}\frac{D_2^2}{\kappa^2}\frac{\kappa}{f^2 + (\kappa/2)^2}$$

Both TRN and GH jitter are therefore negligible for the present measurements, while remaining relevant targets for future cavity-stabilization work.

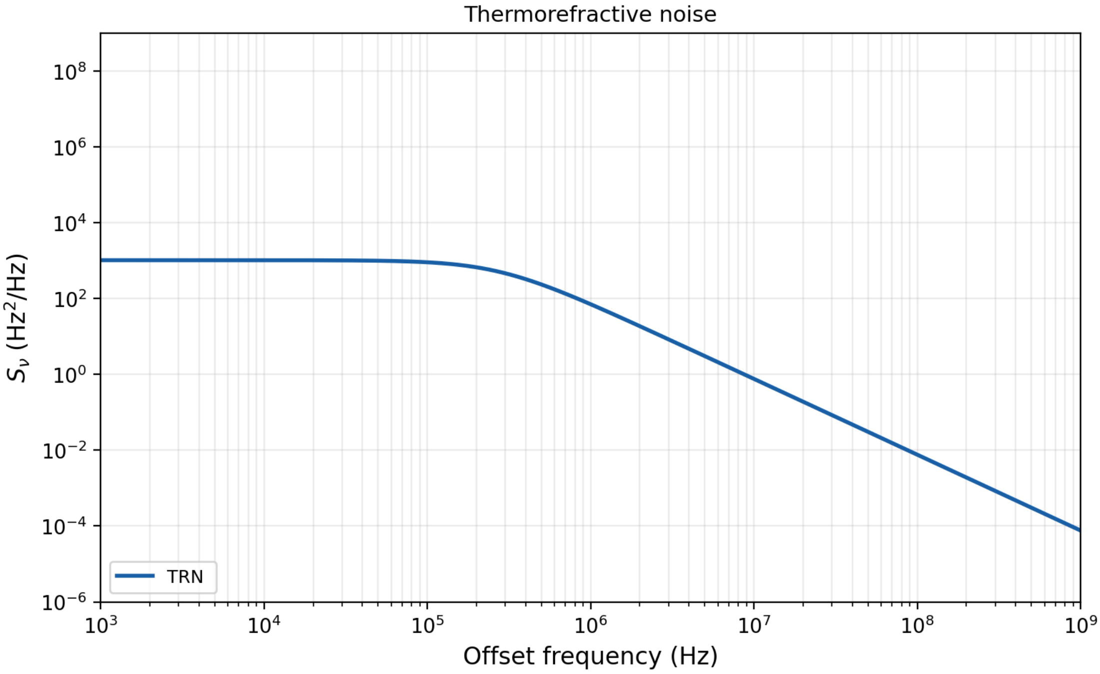


**Figure 2.8:** Estimated thermorefractive noise(in $Hz^2/Hz$) for a ring resonator

## 2.4 2-point optical frequency division

2-point OFD is a mechanism in which the phase noise of the comb teeth of an OFC generated by a pump laser at $\nu_{\text{pump}} = 192.07$ THz is reduced, by injecting an auxiliary laser close to a comb tooth far from the pump. When a comb tooth is present close to the auxiliary laser injected at $\nu_{\text{auxiliary}} = 194.55$ THz, the comb tooth gets phase-locked to the auxiliary laser. This phase locking is then also transferred to the comb teeth present in between the auxiliary laser and the pump laser. The phase noise of the repetition rate $f_{\text{rep}}$ inherits the phase noise of the pump laser reduced by the square of the division ratio as given by Eq. (2.11)[10].

$$\mathcal{L}_{\text{rep}}(f) = \mathcal{L}_{\text{pump}}(f) - 20\log_{10}\left(\frac{\nu_{\text{auxiliary}} - \nu_{\text{pump}}}{f_{\text{rep}}}\right), \tag{2.11}$$

The corresponding 2-point OFD suppression is $20\log_{10}(2.5\,\text{THz}/50\,\text{GHz}) \approx 34\,\text{dB}$, which is the targeted division factor used to define the 2-point OFD limit throughout this thesis.
Equation (2.11) evaluated with the measured pump-laser phase noise serves throughout this thesis as the *2-point OFD limit*: the best repetition-rate phase noise achievable from the targeted optical-to-RF division factor, assuming ideal comb stabilization with no excess noise from the resonator itself. All measured phase noise spectra are compared against this benchmark.
Equation (2.2) shows that constraining the comb grid requires two independent boundary conditions, one for $f_{\text{rep}}$ and one for $f_{\text{CEO}}$. Two-point optical stabilization satisfies this requirement by locking two spectrally separated comb teeth, $\nu_{n_1}$ and

$\nu_{n_2}$, to two independent narrow-linewidth CW references [28], giving

$$f_{\text{rep}} = \frac{\nu_{n_2} - \nu_{n_1}}{n_2 - n_1}. \tag{2.12}$$

Constraining teeth separated by $\Delta n$ modes is therefore equivalent to optically dividing their frequency difference, analogously to Eq. (2.11) but with the division ratio set by $\Delta n$. A key practical advantage is that this scheme requires no $f$-to-$2f$ interferometry , a measurement challenging on microresonator platforms due to limited bandwidth and low per-tooth power.

In this work, one constraint is supplied by the pump laser frequency, which pins the comb grid, while the second is provided by injecting a narrow-linewidth auxiliary CW laser into a chosen comb tooth [28, 29].

For the parameters used in this experiment, pump wavelength $\lambda_{\text{pump}} = 1560.9\,\text{nm}$, auxiliary wavelength $\lambda_{\text{aux}} = 1540.9\,\text{nm}$, and repetition rate $f_{\text{rep}} \approx 49.921\,\text{GHz}$, the spectral separation is $\Delta\nu \approx 2.49\,\text{THz}$, spanning

$$\Delta n = \frac{\Delta\nu}{f_{\text{rep}}} \approx 50 \tag{2.13}$$

comb modes. The expected reduction in the phase noise through 2-point OFD is 34 dB.

## 2.5 Optical injection locking

Directing an external CW field into a resonator sustaining a frequency comb produces qualitatively distinct effects depending on the detuning between the injected field and the nearest comb tooth.

**Within the locking bandwidth** ($\Delta f < \Delta f_{\text{lock}}$), the comb tooth is pulled onto the injected field through *optical injection locking* (OIL) [30, 29, 31]. Once locked, the tooth's instantaneous phase tracks that of the reference, and this coherence propagates to $f_{\text{rep}}$ through the comb equation. For OIL to reduce repetition-rate phase noise, the reference must be quieter than the free-running comb tooth at every Fourier offset within the locking range; if not, OIL adds extra noise.

When the auxiliary laser wavelength is *lesser* than the pump, as in all measurements of this work, it addresses a comb tooth on the high-frequency (blue) side at mode index $n_{\text{aux}} \approx 50$.

## 2.6 Photodetection and measurement noise floor

Recovering the RF repetition rate from the optical comb pulse train requires a photodiode with sufficient bandwidth to respond at $f_{\text{rep}}$. Square-law detection converts incident optical intensity into photocurrent:

$$i(t) \propto |E(t)|^2, \tag{2.14}$$

where $E(t)$ is the optical field envelope incident on the detector. The frequency domain contains RF tones at $f_{\text{rep}}$ and its harmonics; the power in each harmonic

scales quadratically with photocurrent, so maximizing incident optical power (within the diode's linear range) directly improves the RF carrier-to-noise ratio. Multi-soliton states deliver proportionally greater energy per round trip than a single soliton, strengthening the RF carrier accordingly [1]. This carrier enhancement with increasing soliton number plays a central role in interpreting the phase noise results of Chapter 4.
Inserting a frequency divider of ratio $N$ between the source and the analyzer reduces both the carrier frequency and the phase noise by

$$L_{\text{out}}(f) = L_{\text{in}}(f) - 20\log_{10}(N), \tag{2.15}$$

extending the effective dynamic range by $20\log_{10}(N)$ dB. For the factor-of-four divider used in the 12.48 GHz configuration, this yields 12 dB gain in dynamic range. Because ideal division is a coherent linear operation, the phase noise shape and soliton-number dependence are preserved and can be compared directly against the scaled 2-point OFD benchmark.

## Chapter summary

The theoretical framework assembled in this chapter, encompassing DKS physics, coupled-ring supermode formation, the 2-point OFD noise suppression mechanism, and the conditions under which optical injection locking helps or harms repetition-rate purity, provides the complete physical foundation for the experimental work described in Chapter 3.

# 3

# Methods

The experimental work was structured around three sequential phases, each building on the previous one. First, all available CW laser sources' frequency and phase noise were characterized to establish the 2-point OFD limit against which all subsequent results are compared (Section 3.1). Second, a reliable and repeatable procedure was developed for accessing and maintaining multiple distinct soliton states on the photonic molecule chip (Section 3.3). Third, the repetition-rate phase noise was extracted using three RF measurement configurations of progressively increasing dynamic range, each motivated by a specific limitation of its predecessor (Section 3.4). The auxiliary laser injection experiment, motivated by the two-point OFD stabilization scheme introduced in Section 2.4, was embedded within this same experimental framework and is described at the end of the chapter (Section 3.5).

## 3.1 Laser source characterization

All laser sources were characterized before any comb generation work began, as their noise properties directly set the theoretical lower bound on the repetition-rate phase noise achievable via 2-point OFD (see Section 2.4). Table 3.1 lists the three CW sources measured in this work.

**Table 3.1:** CW laser sources characterized in this work.

| Label | Model | Role |
|---|---|---|
| Laser 1 | Toptica CTL 1550 | Pump (primary) |
| Laser 2 | Toptica CTL 1550 | Auxiliary reference |
| Laser 3 | OEwaves OE40XX | Characterization reference |

Frequency noise power spectral densities were recorded using the OEwaves OE4000 laser characterization system. Each laser was measured separately on this system. The OE4000 measurements are used as the reference for all subsequent 2-point OFD calculations in this thesis. The characterization results are presented in Section 4.

## 3.2 Experimental setup

The complete optical and RF measurement configuration is shown in Fig. 3.1. The setup was used throughout all soliton generation and phase noise measurement campaigns. Depending on the measurement phase, not all paths are active simultaneously; the auxiliary path is only engaged during the optical injection experiments (Section 3.5).

Four principal signal paths are present:

- **Pump path:** Toptica CTL → High-Power EDFA (1 W) → polarization controller (PC) → variable optical attenuator (VOA) → 20 dB coupler → photonic molecule chip via lensed fiber. An optical power meter (OPM) positioned after the 20 dB coupler monitors the coupled pump power in real time.
- **Auxiliary path:** 2nd Toptica CTL → pre-amplifier EDFA → PC → VOA → 10 dB coupler → 3 dB coupler → chip. This path delivers the auxiliary reference laser to the target comb tooth for optical injection and is engaged only during the experiment described in Section 3.5.
- **Output path:** chip output → 10 dB coupler → 20 dB coupler → 80/20 splitter. The 80 % port feeds the 50 GHz photodetector (PD); the 20 % port is fed to a tunable fiber Bragg grating (FBG) for filtering the CW pump and ASE. The drop port of this filter is intended to contain the CW pump and ASE(also referred to in this thesis as Transmitted Power). The through port of the filter contains the OFC with the CW pump line heavily attenuated(also referred to as Converted Power in this thesis). The converted power from the through port of the FBG filter, and the transmitted power from the drop port of the filter are then sent separately to two Thorlabs 5 GHz PDs, for monitoring them on the oscilloscope. The converted power is then fed at the input of the Digital Laser Controller(DLC) of the pump laser for performing PID loop locking using the DLC.
- **RF chain:** 50 GHz PD → DC block → RF LNA (ADL8106) → optional ÷4 divider (AT-FDN-54AS2-FD) → R&S FSWP phase noise analyser or electrical spectrum analyzer (ESA).

The chip rested on a temperature-controlled stage incorporating a Peltier module. Thermal stabilization was achieved with a PID controller whose setpoint corresponded to an NTC thermistor resistance of 11.557 kΩ.

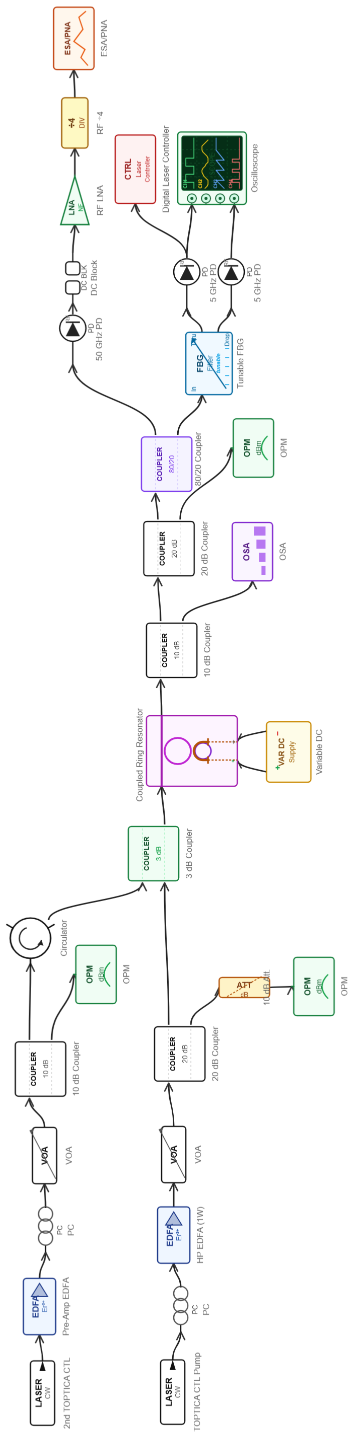


htbp

**Figure 3.1:** Schematic of the optical and RF measurement setup. The pump path (lower) drives the coupled micro-ring resonator. The auxiliary laser path (upper) provides the optical injection reference and is only active during the injection experiment (Section 3.5). The comb output is directed to the 50 GHz photodetector for RF extraction and to the OSA for spectral monitoring. Note: Unless otherwise explicitly mentioned to be different in the RF path, this is the schematic for all the measurement results given in the Results Section.

## 3.3 Microcomb generation

A reproducible soliton generation sequence was developed iteratively and ultimately codified into the ten-step procedure described below. Each step was found to be necessary for reliable access to a target soliton number. Steps 1-8 bring the system into a stable multi-soliton DKS state; Steps 9 and 10 describe how to reduce the number of circulating solitons further, with Step 10 specifically targeting the single-soliton state.

1. **Setting the input pump laser optical power.** The VOA in the pump laser path was adjusted such that the on-chip CW pump power was 16.5 dBm.
2. **Locate the avoided mode crossing.** The pump wavelength was scanned across successive resonances while the auxiliary-ring heater voltage was incremented within a certain voltage range at each of these resonances, while the drop-port power was monitored on an oscilloscope. A particular main-ring resonance was selected if tuning the auxiliary-ring heater voltage caused an AMX, which manifests as a characteristic splitting of the single resonance dip into two closely spaced features as observed on the monitored drop port power(see Figure 2.7). This splitting confirms that the coupled-supermode condition has been reached.
3. **Optimize polarization alignment.** The three paddles of the pump-path polarization controller were adjusted iteratively to maximize the resonance extinction ratio visible on the oscilloscope transmission trace, ensuring that the coupled pump field is aligned to the TE mode of the bus waveguide and maximizing intracavity power build-up.
4. **Align the tunable FBG filter.** The tunable Fiber Bragg Grating filter's center wavelength was adjusted to maximize the pump signal at the drop port while centering this filtered pump within the pump EDFA's(referring to the High-Power EDFA in the pump laser's path) ASE spectrum.
5. **Set the pump laser frequency higher than resonance frequency.** The pump laser was detuned to a frequency slightly higher than the target resonance frequency.
6. **Sweep through the resonance to initiate comb formation.** The pump frequency was slowly decreased to a value closer to the resonance frequency while the OSA was monitored for the appearance of primary comb lines at a greater spacing corresponding to the modulation-instability regime and precedes coherent soliton formation.
7. **Lock the pump laser using DLC.** Once the pump was positioned at a suitable operating point on the converted power trace, frequency stabilization was established through side-of-fringe locking Software utility of the DLC: the converted power serves as the input signal to the laser's DLC's PID controller (the second PID loop, which actuates the piezo-electric control in the DLC's interface) to maintain the pump at a fixed point on the converted power trace. Successful locking was confirmed by observing the OSA and making sure the MI primary comb remains after enabling the PID loop.
8. **Step down the soliton number using the auxiliary-ring heater.** A DC bias voltage was applied to the integrated resistive heater on the aux-

iliary ring, thermally shifting its resonance frequency. Incrementally raising this voltage initially transforms the MI primary comb to a chaotic comb(as observed on the OSA) and a very noisy repetition rate beat note(as observed on the ESA), and on further incrementing transforms the chaotic comb to a Multi-soliton(example 7 solitons or higher) comb with a stable and low noise repetition rate beat note. Further incrementing the voltage collapses the intracavity soliton population one soliton at a time [1]. Using this technique, states containing two through seven solitons were each accessed and held individually, with each step marked by a discrete reduction in transmitted optical power.

9. **Confirm the soliton number.** Each target state was verified through two independent signatures. On the OSA, a single-soliton state displays a clean, $\text{sech}^2$ spectral envelope; multi-soliton states exhibit a periodically amplitude-modulated $\text{sech}^2$ envelope whose ripple period encodes the inter-soliton angular separation inside the ring [1]. On the ESA, all confirmed soliton states produced a single narrow repetition-rate tone. Optical spectra for all accessed soliton states are provided in Section 4.2. In this work, direct temporal characterization of the intracavity pulse train was not performed.
10. **Accessing the single-soliton state.** Unlike the heater-based reduction in Step 8, the single-soliton state was reached from a low-order multi-soliton condition by gradually reducing either the pump power via the VOA or the lock set-level of the pump laser controller, until the OSA displayed a clean, $\text{sech}^2$ envelope characteristic of a single circulating pulse.

## 3.4 Phase noise measurement methods

Three different RF configurations were used to characterize the repetition-rate phase noise, each motivated by a specific limitation of its predecessor. The results obtained with each configuration are presented in Section 4.

### 3.4.1 Down mixing to 279 MHz

In the first configuration, an electro-optic intensity modulator driven by a 25.1 GHz local oscillator (LO) was used to downconvert $f_{\text{rep}}$ to a beat frequency near 279 MHz, within the pass-band of a standard ESA. This configuration was intended to exploit the lower instrument noise floor available at sub-gigahertz carrier frequencies. Although the target beat tone appeared at the expected frequency ($f_{\text{rep}} - 2 \times 25.1\,\text{GHz} \approx 279\,\text{MHz}$), the available LO produced a dense forest of spurious tones throughout the spectrum that prevented reliable phase noise extraction. This approach was abandoned in favor of direct high-frequency detection.

### 3.4.2 Direct measurement at 49.921 GHz

The second configuration directed the output of the 50 GHz PD directly into the R&S FSWP phase noise analyzer after amplification by a wide-band RF LNA, with

no optical amplification in the output path. The RF carrier power at the FSWP input was approximately −16 dBm.
An EDFA was subsequently inserted into the optical output path to raise the photodetected power and the RF carrier level to approximately −10 dBm. Although this extended the dynamic range at high offset frequencies, the EDFA also introduced ASE that significantly degraded the close-in phase noise below 1 kHz offset, precisely the region most relevant for comparison against the 2-point OFD benchmark (see Section 4.2). The EDFA was therefore removed from the output path for all subsequent measurements.

### 3.4.3 Frequency division to 12.48 GHz

To extend dynamic range without reintroducing optical amplification, the amplified RF signal from the LNA was passed through a factor-of-four frequency divider, reducing the carrier frequency to approximately 12.48 GHz. Electronic frequency division by $N$ reduces the SSB phase noise of the output relative to the input by $20 \log_{10}(N)$, a consequence of the phase scaling in the division process [32]; for $N = 4$ this yields a 12 dB improvement in effective measurement dynamic range. Because frequency division is a deterministic frequency-scaling operation, the offset-dependent (sloped) phase-noise components preserve both their spectral shape and soliton-number dependence while being reduced by the expected $20 \log_{10}(N)$ factor (here, $N = 4$). White phase-noise components already present on the signal are similarly reduced by this factor. However, the thermally limited white phase-noise floor observed in the measurement is ultimately determined by additive thermal and electronic noise introduced by the frequency divider, amplifiers, and phase-noise analyzer. These additive noise contributions are not suppressed by the division process and therefore establish the residual measurement floor. Consequently, the full 12 dB improvement is realized only while the measurement remains limited by the signal phase noise rather than by the instrumentation noise floor. The divided-down trace can therefore be compared directly against the correspondingly scaled 2-point OFD benchmark, while also noting that the FSWP analyzer provides a superior dynamic range at 12.5 GHz compared to direct measurements at 50 GHz [33, 34].

## 3.5 Optical injection locking procedure

The auxiliary laser injection experiment was performed after a stable soliton state had been established following the procedure of Section 3.3, with the goal of evaluating whether two-point OFD stabilization (Section 2.4) could be achieved. The procedure brought the auxiliary laser into optical injection with the nearest comb tooth in five steps:

1. **Coarse wavelength alignment.** The auxiliary laser wavelength was placed approximately midway between comb teeth $n - 1$ and $n + 1$ on the OSA, at a detuning of several hundred megahertz from the nearest tooth at $n$.
2. **Monitor the heterodyne beat.** The RF beat between the auxiliary laser and the nearest comb tooth $n$ was observed on the ESA, configured with a 500 MHz center frequency and 1 GHz span.

3. **Reduce the detuning.** The auxiliary laser piezo voltage was swept to drive the heterodyne beat frequency monotonically toward 0 Hz.
4. **Identify the injection regime.** Two outcomes were possible. If the beat note collapsed entirely, OIL had been achieved and the comb tooth had locked phase-coherently to the auxiliary field. If the beat persisted at a reduced frequency without collapsing, the system was in the sub-threshold optical injection (OI) regime. For the Toptica CTL auxiliary source, OIL consistently degraded the repetition-rate RF spectrum (see Section 4.2.1); the sub-threshold OI regime was therefore explored as an alternative.
5. **Record the phase noise.** The repetition-rate phase noise was recorded on the FSWP at the appropriate carrier frequency under both injection and pump-only conditions, with all other experimental parameters held constant to permit direct comparison.

# 4

# Results and discussion

The chapter opens with the laser source characterization that establishes the 2-point OFD benchmark used throughout (Section 4.1). The optical spectrum of the soliton states and the electrical spectrum of the repetition rate beat note produced by multi-soliton states generation results are then reported, followed by the repetition-rate phase noise measurements at 50 GHz (Section 4.2) and at 12.48 GHz after electronic frequency division (Section 4.3). The chapter closes with a unified physical interpretation of the three central experimental findings: the degradation introduced by auxiliary laser injection, the change in the expected repetition rate phase noise behavior of multi-soliton and single soliton states, and the marginal deviation from the 2-point OFD model (Sections 4.4–4.5).

## 4.1 Laser source frequency and phase noise

The two Toptica CTL pump and auxiliary lasers were characterized on the OE-4000 Phase Noise and Linewidth Analyzer before any comb generation work began, establishing the optical noise baseline from which the 2-point OFD prediction is derived.

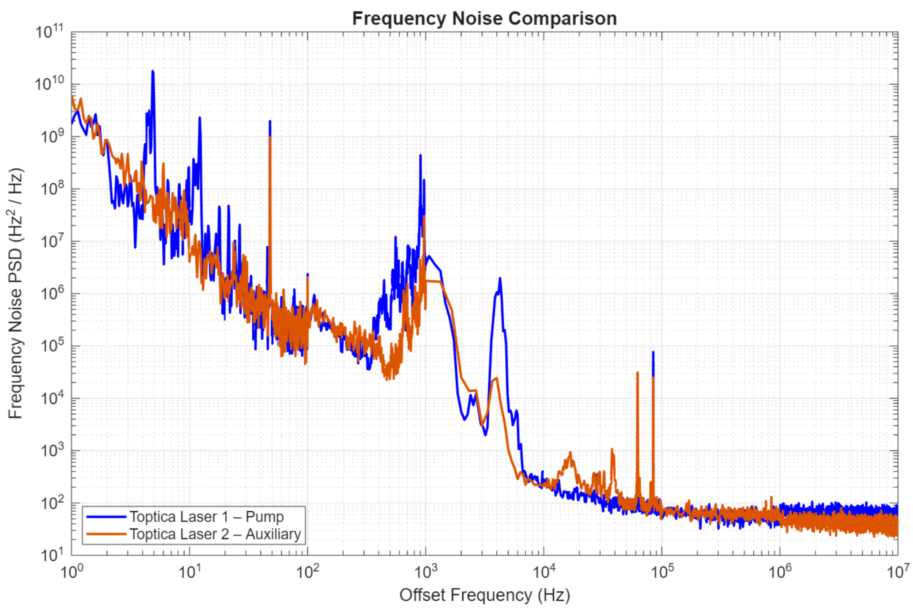


**Figure 4.1:** Frequency noise PSD of the two Toptica CTL CW laser sources (Laser 1 as pump, Laser 2 as auxiliary) measured independently on the OE4000 system.

Figure 4.1 shows the measured frequency noise PSDs of both Toptica CTL lasers. The two units of the same model exhibit broadly similar noise characteristics across the full offset range, as expected for matched hardware.

To get the 2-point OFD benchmark, the measured pump-laser phase noise was scaled by the nominal suppression factor of approximately 34 dB as mentioned in Section 2.4. This scaled trace is used throughout the chapter as the theoretical 2-point OFD reference against which all measured repetition-rate phase noise spectra are compared.

Figure 4.2 compares the 2-point OFD-scaled pump phase noise with the ADF5611 electronic PLL reference at 12.5 GHz (performance taken from the ADF5611 data sheet [2]). The comparison shows that optical frequency division should, in principle, outperform the electronic reference at offsets greater than 10 kHz, motivating the use of the photonic molecule microcomb as a low-noise microwave source. The phase-noise contribution arising from photodiode shot noise was estimated for the maximum photocurrent that could be applied to the 50 GHz photodiode without driving it into saturation. Under these conditions, the corresponding shot-noise floor was calculated to be −145 dBc/Hz.

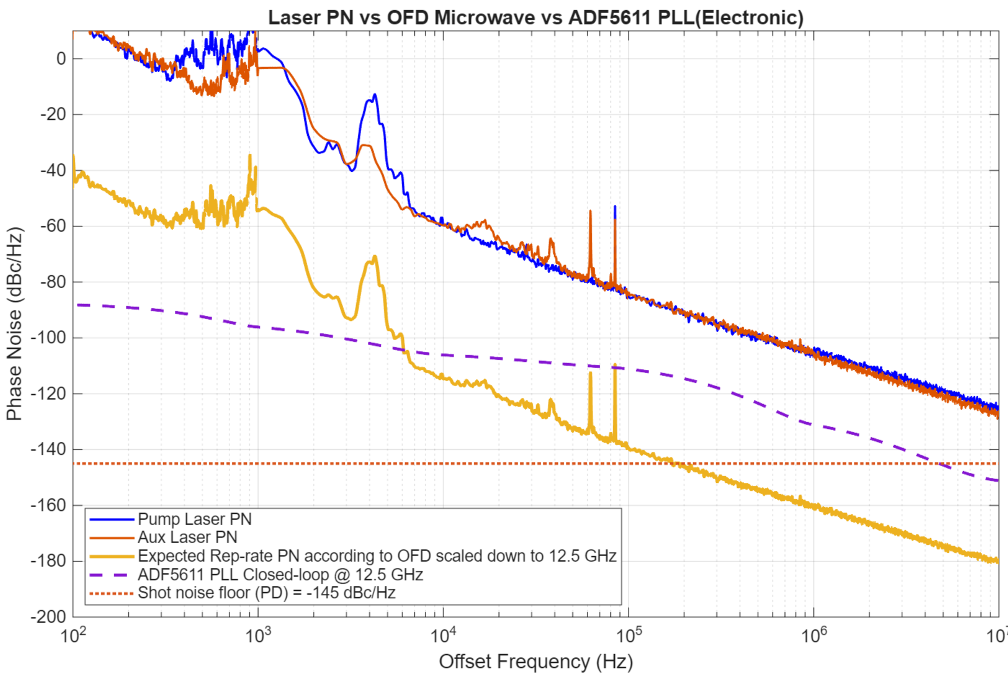


**Figure 4.2:** Pump-laser phase noise scaled by 34 dB 2-point OFD suppression factor (yellow) and compared against EVAL-ADF5611 electronic VCO/PLL reference at 12.5 GHz (dashed purple, Note: This plot is generated by extrapolating the phase noise data from 14.4 GHz given in [2]), together with the raw pump-laser (blue) and auxiliary-laser (orange) phase noise traces. This scaled trace serves as the 2-point OFD benchmark throughout the chapter. The shot noise contribution of the 50 GHz photodiode to the phase noise(dashed orange) trace is calculated based on the maximum photocurrent that can be coupled to the photodiode such that the photodiode stays in the linear region.

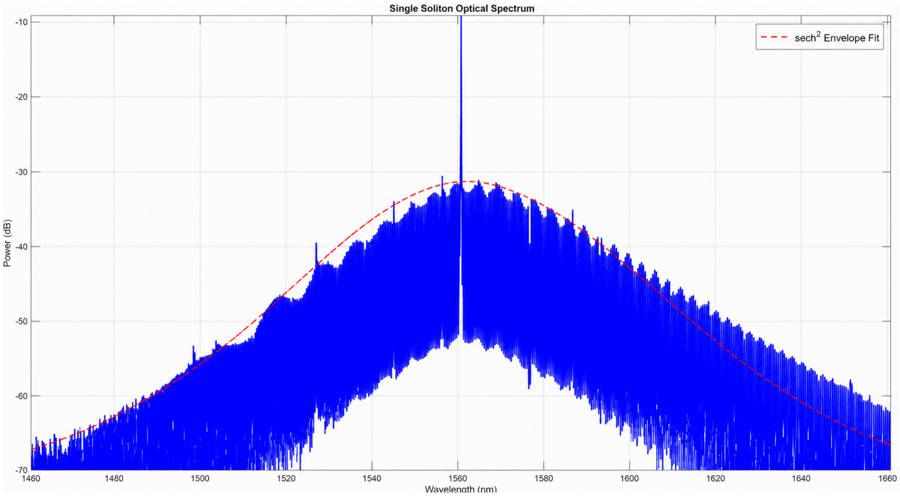


**(a)** Optical Spectrum of the single soliton state

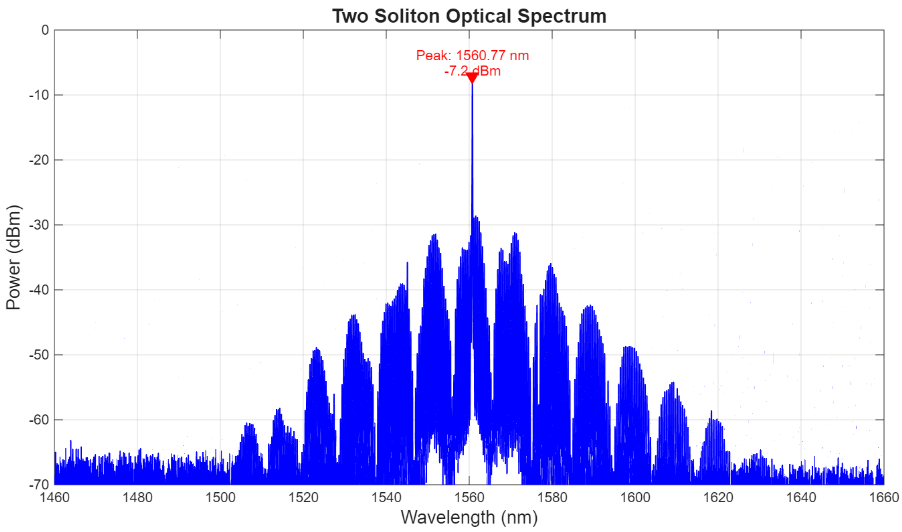


**(b)** Optical Spectrum of the two soliton state

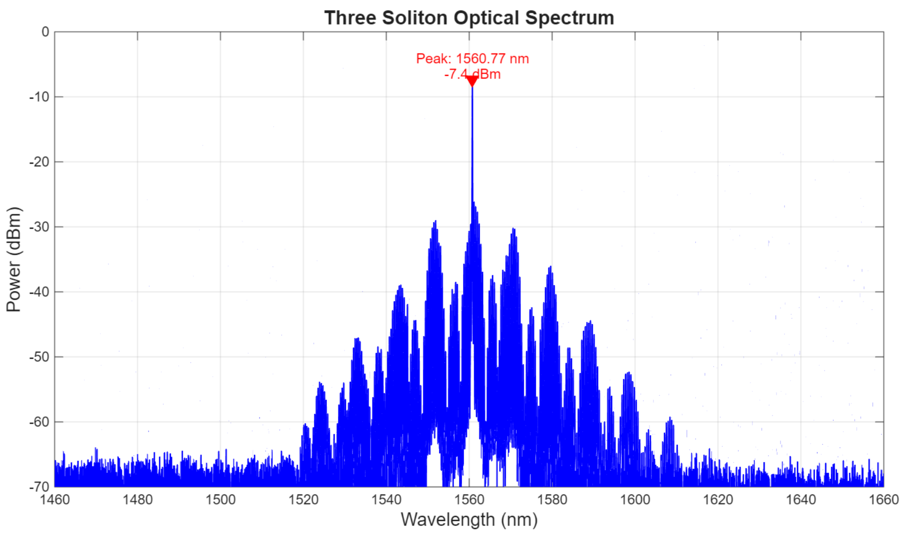


**(c)** Optical Spectrum of the three soliton state

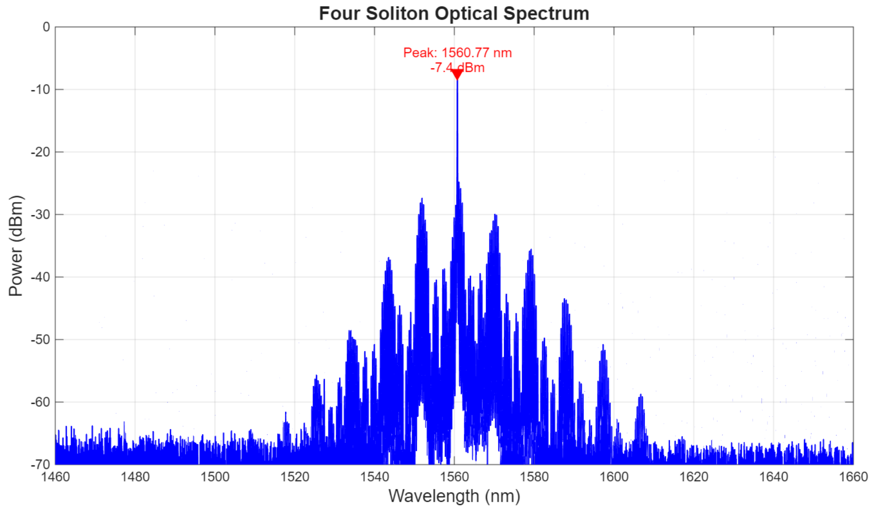


**(d)** Optical Spectrum of the four soliton state

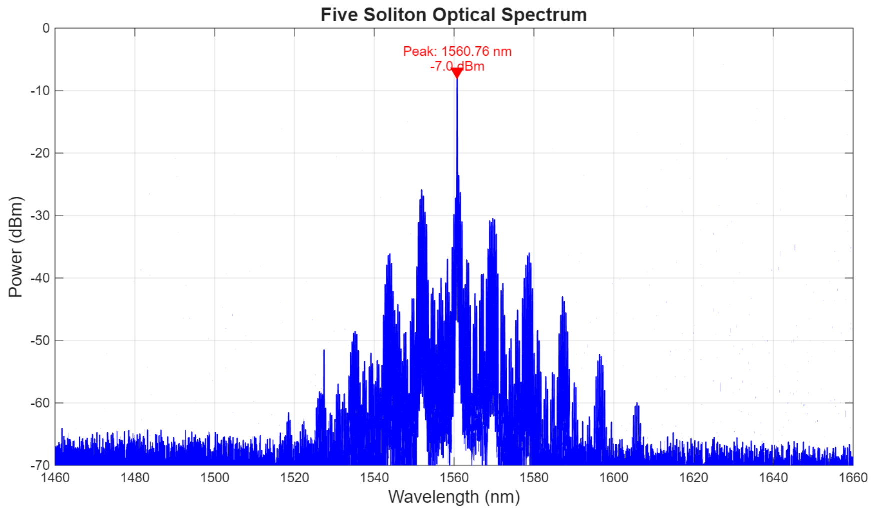


**(e)** Optical Spectrum of the five soliton state

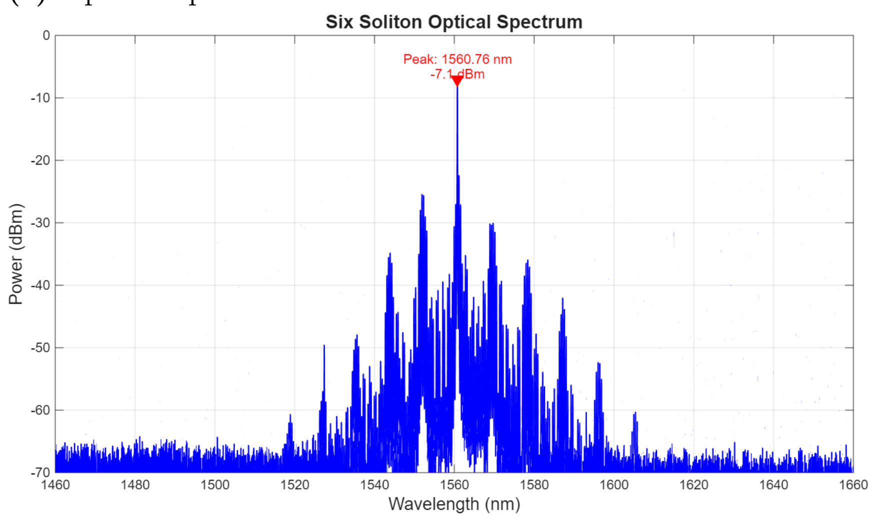


**(f)** Optical Spectrum of the six soliton state

**Figure 4.3:** (a), (b), (c), (d), (e), (f) Optical Spectrums of Soliton States generated using a coupled ring resonator.

## 4.2 Phase noise: direct detection at 50 GHz

The transition from chaotic comb generation to stable soliton generation was monitored simultaneously on the OSA and ESA. Figure 4.3 presents the optical spectra captured on the OSA for each of the seven soliton states accessed during the experiment. All spectra were acquired with identical OSA settings (resolution bandwidth 0.05 nm, sensitivity mode MID, averaging disabled) on the Yokogawa AQ6370D Optical Spectrum Analyzer.

The electrical spectrum of the repetition-rate beat note produced for all multi-soliton states at $f_{\mathrm{rep}}$ is shown in Fig. 4.4. For the 6-soliton state, the RF carrier power at the Agilent N9030A PXA Signal Analyzer input was approximately −16 dBm. Under these conditions, the corresponding phase-noise measurement shown in Fig. 4.5 (no-EDFA trace) approaches the analyzer noise floor at offset frequencies above approximately 30 kHz, indicating the onset of the instrument-limited measurement regime.

Below approximately 10 kHz, the soliton phase noise is clearly resolved and follows an approximately $f^{-2}$ slope in log–log scale, consistent with white frequency noise transferred from the pump laser. No pronounced excess-noise feature was observed near 1 kHz, a behavior that is addressed in Section 4.4.

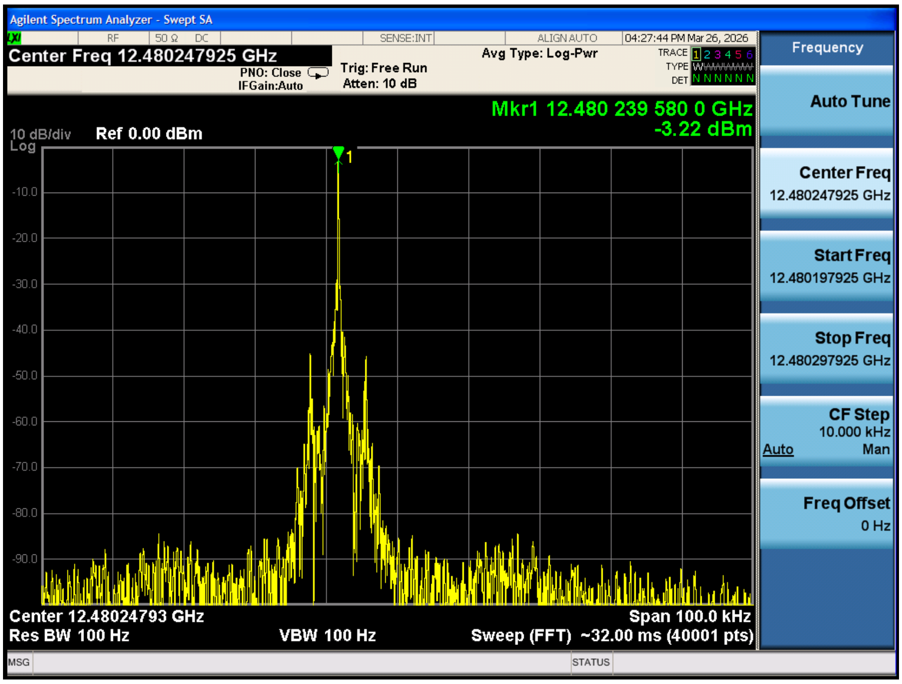


**Figure 4.4:** ESA spectrum of the $f_{\mathrm{rep}}$ beat note of a multi-soliton state, showing a clean narrow tone.

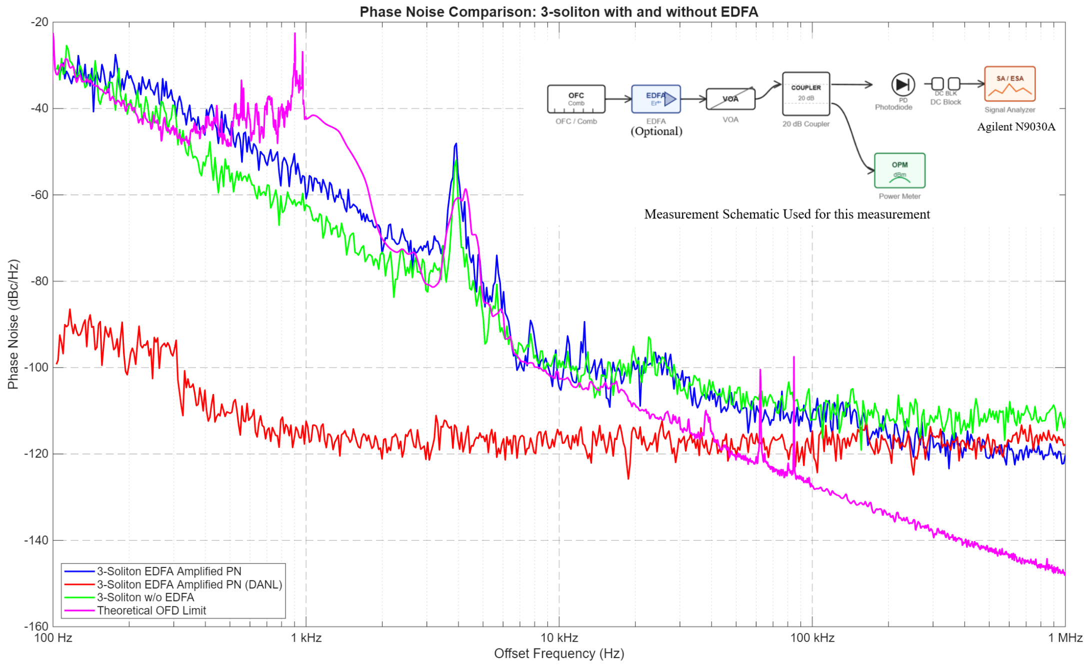


**Figure 4.5:** Phase noise comparison at 49.921 GHz of a 3-soliton state without the EDFA (green) and with the EDFA (blue) inserted in the optical output path, measured using the Agilent N9030A PXA Signal Analyzer. The red trace plots the displayed average noise level(DANL) of this measurement. The EDFA improved the high-offset noise floor but degrades close-in phase noise below 1 kHz, where comparison against the theoretical 2-point OFD limit (pink) matters most. Shown in the inset is the measurement schematic used.

To try to extend the instrument-noise-free window toward higher offset frequencies, an EDFA was inserted into the optical output path to raise the photodetected power. The detected RF tone increased from approximately $-20$ dBm to $-10$ dBm, extending the available analyzer dynamic range. While the stronger RF carrier shifted the onset of instrument-noise-limited behavior to higher offsets, as shown in Fig. 4.5, the EDFA simultaneously introduced amplified spontaneous emission that measurably degraded the phase noise below 1 kHz, precisely the low-offset region most important for comparison against the 2-point OFD benchmark. The EDFA was therefore excluded from all subsequent phase-noise measurements.

### 4.2.1 Influence of number of solitons and auxiliary injection on phase noise

The most significant experimental findings of this work emerged from comparing phase-noise behavior across soliton numbers. The ensuing phase noise measurements used the R&S FSWP Phase Noise Analyzer(PNA). Figure 4.6 extends the comparison to the full set of soliton numbers measured on the R&S FSWP. The phase noise of the 1-soliton state consistently gave the highest phase noise of all states characterized, in contrast to the trend commonly observed in conventional single-ring microresonators. Notably, both the 3-soliton and 5-soliton states exhibit measurably lower phase noise than the 1-soliton state across the accessible offset range, and this ordering was reproducible across repeated measurements. This inversion of the commonly reported single-ring hierarchy is one of the central experimental findings of this thesis and is discussed further in Section 4.4.

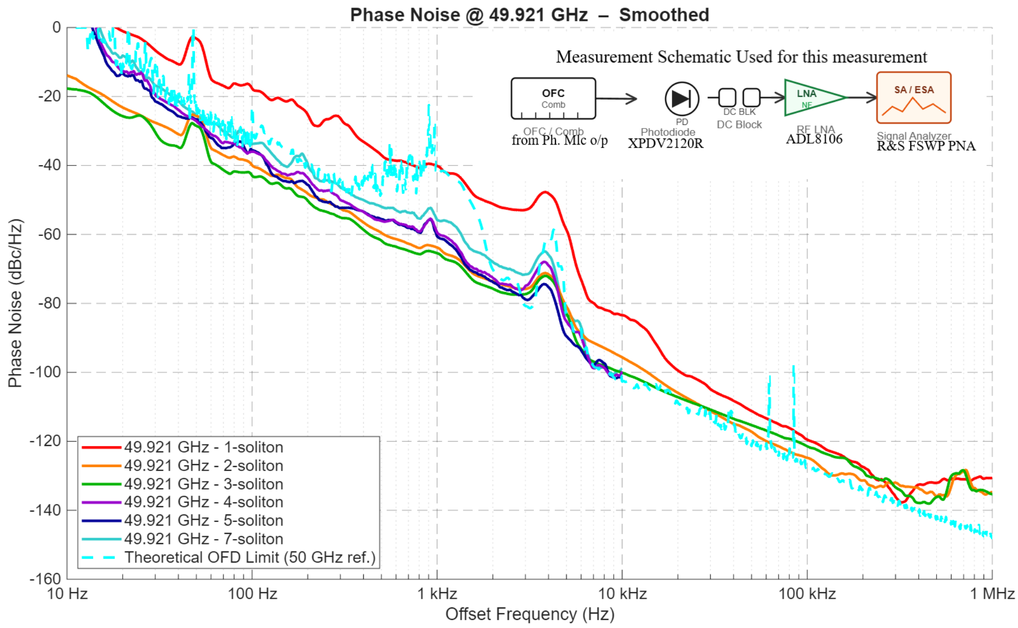


**Figure 4.6:** Phase noise measured at 49.921 GHz for multiple soliton numbers using the R&S FSWP. The theoretical 2-point OFD limit (blue dashed) is shown for reference. Higher soliton numbers consistently outperform the single-soliton state. The frequency axis extends to 1 MHz to capture the full transition to the white noise floor. Note: The phase noise of 4, 5 and 7-soliton states were only measured until 10 kHz. Shown in the inset is the measurement schematic used.

**Effect of auxiliary laser injection.** Auxiliary laser injection consistently degraded the repetition-rate phase noise relative to the pump-only case for every soliton state tested. Rather than stabilizing $f_{\text{rep}}$, the auxiliary path broadened the RF beat note and raised the phase noise floor across the entire measured offset range. The mechanism behind this degradation is explained in Section 4.4 and is summarized here as a direct consequence of the auxiliary laser's noise.

## 4.3 Phase noise: division to 12.48 GHz

The amplified RF signal was passed through a factor-of-four divider, which in turn was input to a PNA, reducing the carrier to 12.48 GHz and gaining 12 dB of effective dynamic range as per Equation (2.15).

Figure 4.7 shows the phase noise of the three-soliton state measured at 12.48 GHz. The $f^{-2}$ slope is preserved after division, confirming that the dominant noise process is unchanged. The trace remains close to the 2-point OFD benchmark until approximately 100 kHz, beyond which the floor flattens due to the combined contributions of photodiode shot noise, LNA thermal noise, and divider-added noise.

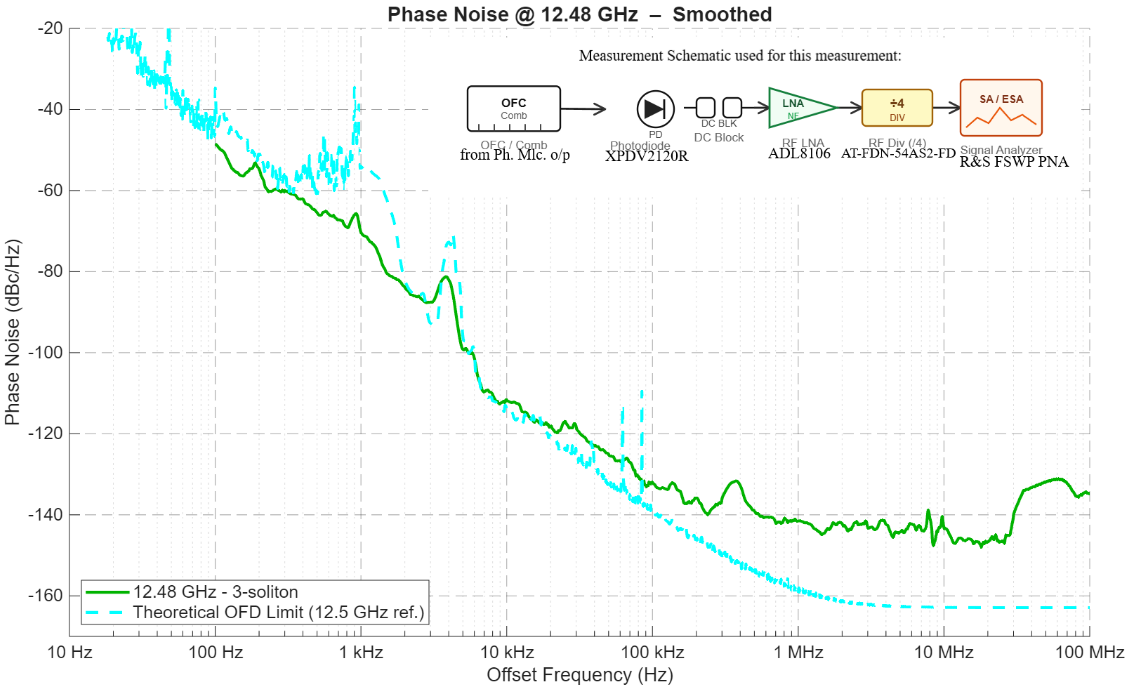


**Figure 4.7:** Phase noise measured at 12.48 GHz for the 3-soliton state (solid green), together with the theoretical 2-point OFD limit scaled to 12.5 GHz (dashed blue). There is a 12 dB reduction in phase noise relative to the 50 GHz measurements. Shown in the inset is the measurement schematic used.

## 4.4 Physical interpretation of the measured phase noise

Three observations distinguish the photonic molecule microcomb studied here from a conventional single-ring 2-point OFD system: (i) the best measured phase-noise traces approached or marginally surpassed the nominal 2-point OFD benchmark without exhibiting the excess-noise feature predicted near 1 kHz offset, (ii) higher-order soliton states outperformed the single-soliton state, and (iii) auxiliary laser injection degraded rather than improved the repetition-rate phase noise.
These observations are interpreted here in the context of the coupled-ring (photonic molecule) architecture introduced in Section 2.2. In contrast to a single microring, the coupled micro-ring resonator contains an auxiliary ring coupled to the main resonator, producing hybridized supermodes and an AMX near the pump wavelength. This AMX modifies both the local dispersion and the effective resonance lineshape experienced by the pump field. The following paragraphs discuss how these coupled-ring-specific features plausibly influence repetition-rate phase noise.
1) The higher soliton numbers exhibited lower phase noise.
In conventional single-ring microresonators, the single-soliton state is commonly the lowest-noise operating point because it minimizes intracavity power and therefore reduces thermorefractive noise coupling and thermal instability [19].
The coupled microring resonator showed the opposite trend: two, three- and five-soliton states consistently outperformed the single-soliton state by approximately

5-10 dB across the offset range.
Part of this improvement is explained as follows: Multi-soliton states contain greater total intracavity pulse energy and therefore deliver higher optical power to the photodetector, increasing the RF carrier power at $f_{\mathrm{rep}}$ and improving the measured carrier-to-noise ratio [1].
A second mechanism may be specific to the coupled-ring architecture. The AMX locally perturbs the modal dispersion near the pump wavelength by modifying the supermode frequencies and intracavity field distribution [35]. In a multi-soliton state, this may create preferred angular positions or relative separations for co-propagating solitons, effectively acting as a weak pinning potential.
If present, this pinning would suppress slow drift of relative soliton positions, which otherwise contributes timing fluctuations to the repetition rate.
This interpretation remains a hypothesis and would require numerical simulations for direct verification.
2) The phase noise of the repetition rate of a comb generated with just a pump laser is already lower than a two point OFD stabilised comb using in addition an auxiliary laser(i.e. two point OFD was theoretically supposed to be the only way to lower phase noise, but this work has shown that without doing two point OFD, the phase noise can be suppressed using a single laser and a coupled ring resonator).
2-point OFD, introduced in Section 2.4, describes transfer of optical phase stability to the microwave repetition rate through the comb relation. Under the ideal assumption of a passive noiseless divider, the repetition-rate phase noise is given by Eq. (2.10).
This model assumes: (i) the pump laser phase noise is transferred uniformly to the repetition rate after scaling by the optical-to-microwave division ratio, and (ii) the resonator itself does not introduce additional frequency-dependent shaping of the transferred noise.
These assumptions provide a useful first-order benchmark but are not guaranteed to hold for the coupled-ring resonator studied here.
Unlike a conventional single-ring resonator, the photonic molecule contains an avoided mode crossing (AMX) produced by coupling between the main and auxiliary rings. This hybridization modifies the effective resonance lineshape and intracavity field distribution seen by the pump [35].
As a result, pump phase fluctuations may not be transferred uniformly into the comb repetition rate's phase noise across all Fourier offsets. Instead, the coupled resonator may act as a frequency-dependent transfer element, selectively suppressing certain components of pump noise before they are converted into repetition-rate fluctuations [36, 37].
Experimentally, the phase-noise feature predicted near 1 kHz by simple 2-point OFD scaling was absent in every measured spectrum, and the best traces lay marginally below the nominal 2-point OFD benchmark.
Taken together, these observations suggest that the coupled-ring resonator modifies the transfer of pump noise to the repetition rate in a way not captured by the ideal 2-point OFD model.
This interpretation is intentionally conservative: the present measurements have not taken into account the phase noise of the individual comb teeth of the OFC generated

by the coupled ring resonator, and dedicated modelling would be required to verify the mechanism quantitatively.
3) The optical injection locking degraded phase noise.
The auxiliary laser was introduced to implement a two-point stabilization scheme, in which the pump constrains one comb degree of freedom while a second optical reference constrains an additional comb tooth (Section 2.4).
In principle, this should have reduced the phase noise. Experimentally, the opposite behavior was observed: auxiliary injection consistently broadened the RF beat note and increased repetition-rate phase noise.
This could be attributed to the auxiliary laser being injected at a wavelength lesser than the pump laser wavelength. So it is suspected that the OIL of an auxiliary laser at a wavelength higher than the pump laser could reduce the phase noise.

## 4.5 Passive phase noise filtering in coupled microring resonators

In practice, the intracavity field evolves according to the resonator transfer function and nonlinear cavity dynamics. Consequently, phase fluctuations of the pump are not necessarily transferred equally at all Fourier frequencies [38, 36, 37].
For the photonic molecule used here, the AMX introduces additional spectral structure through supermode hybridization, modifying the effective resonance response relative to a single ring resonator's resonance.
This makes it plausible that the coupled-ring device selectively attenuates or reshapes certain pump-noise components before they are converted into repetition-rate fluctuations.
Experimentally, no excess-noise feature was observed near the 1 kHz offset where the nominal 2-point OFD benchmark predicts one.
The absence of this feature, is consistent with the hypothesis that the coupled-ring architecture modifies pump-noise transfer in a way that filters the phase noise.
A quantitative transfer-function measurement is beyond the scope of this work, but the results motivate future investigation of coupled-resonator noise shaping.

# 5

# Conclusion

This work experimentally characterized the repetition-rate phase noise of a $Si_3N_4$ photonic molecule microcomb operated as a microwave source through optical frequency division.

Three principal conclusions emerge.

**First, higher-order soliton states had a lower phase noise.** The result suggests that coupled-ring architectures can alter the conventional soliton-noise hierarchy through mechanisms unavailable in single cavities, including enhanced RF carrier power and potentially AMX-mediated stabilization of multi-soliton states.

An additional factor that may contribute to the observed differences is amplitude-to-phase (AM-to-PM) noise conversion in the photodetection process, which is known to depend sensitively on photocurrent. Since different soliton states generate different optical powers and photocurrents, variations in AM-to-PM conversion may have influenced the measured phase-noise performance and should be investigated separately in future work.

**Second, the phase noise of the repetition rate of a comb generated with just a pump laser is ALREADY lower than a two point OFD stabilized comb using in addition an auxiliary laser(i.e. two point OFD was theoretically supposed to be the only way to lower phase noise, but this work has shown that without doing two point OFD, the phase noise can be suppressed using a single laser and a coupled ring resonator).** This is noteworthy because Equation (2.10) is commonly used as the expected noise limit for ideal optical frequency division.

The presented results suggest that coupled-resonator architectures may modify the transfer of pump noise to the repetition rate through frequency-dependent cavity dynamics not captured by the two-point OFD model.

This matters because it indicates that resonator design may influence phase-noise performance beyond simply setting the repetition rate or conversion efficiency. Coupled-resonator geometries may therefore offer an additional degree of freedom for phase-noise engineering in integrated microwave photonics.

**Third, auxiliary optical injection degraded rather than improved phase noise.** This demonstrates that two-point stabilization is not automatically beneficial. Its success depends critically on the auxiliary reference outperforming the target comb tooth in phase noise.

This finding is practically important because it defines a concrete experimental requirement for future implementations of two-point OFD using coupled microring resonators.

**Comparison with the field.** The best phase noise achieved here, approximately

−130 dBc/Hz at 10 kHz offset, −140 dBc/Hz at 500 kHz offset for the 3-soliton state at 12.48 GHz, is comparable to reported $Si_3N_4$ microcomb oscillators [14] and lies within 6-8 dB of the best chip-scale two-point OFD demonstrations.
System-level evaluation using an Ericsson 5G testbed yielded a best SNIR of 26 dB, compared with 32 −34 dB from conventional electronic local oscillators.
The remaining gap is attributed primarily to RF-chain limitations rather than the soliton oscillator itself, indicating that the photonic source is already competitive at mid and far offsets but limited by downstream detection and RF electronics.

# Outlook

The next objective is to close the remaining system-level performance gap and evaluate whether coupled-resonator microcombs can become deployable low-noise RF sources.
A priority experiment is repeating the two-point stabilization scheme using the OEwaves self-injection-locked laser as the auxiliary source. Its substantially lower phase noise should allow a fair test of whether two-point OFD can genuinely improve repetition-rate stability in this platform.
More broadly, the results motivate further study of coupled-resonator noise filtering. A related direction is the systematic investigation of AM-to-PM noise conversion during photodetection. Because the AM-to-PM conversion coefficient depends on operating photocurrent, different soliton states may experience different levels of amplitude-noise transfer into the measured microwave phase noise. Future experiments should therefore optimize the photodiode operating point independently for each soliton state and quantify the contribution of AM-to-PM conversion to the observed phase-noise differences.
If AMX-induced filtering and soliton stabilization are confirmed, photonic molecules may offer a route to phase-noise performance beyond the limits currently observed in single ring resonators which require two point OFD to reduce the phase noise.
In the long term, monolithic integration of the full optical and RF chain remains the natural target for compact low-noise millimeter-wave generation.

# Bibliography

[1] Ó. B. Helgason. *High-efficiency dissipative Kerr solitons in microresonators*. PhD thesis, Chalmers University of Technology, 2022. ISBN 978-91-7905-647-6.

[2] Analog Devices. ADF5611 integer-$n$ pll with integrated vco data sheet, 2022. URL `https://www.analog.com/en/products/adf5611.html`. Accessed May 2026.

[3] Vladimir Iltchenko, Rabi Wang, Michael Toennies, and Andrey Matsko. Compact high-Q Ka-band sapphire distributed Bragg resonator. *Journal of Applied Physics*, 135(14):144502, 2024. doi:10.1063/5.0195051.

[4] Z. Zhang, X. Zou, Q. Li, and N. Wei. Towards 100 Gbps over 100 km: System design and demonstration of E-Band millimeter wave communication. *Sensors*, 22(23):9514, 2022. doi:10.3390/s22239514.

[5] P. Noel and M. Klemes. Doubling the through-put of a digital microwave radio system by the implementation of a cross-polarization interference cancellation algorithm. In *2012 IEEE Radio and Wireless Symposium*, pages 363–366, Santa Clara, CA, USA, 2012. doi:10.1109/RWS.2012.6175360.

[6] A. Goldsmith. *Wireless Communications*. Cambridge University Press, 2005.

[7] Xingchen Ji, Samantha Roberts, Mateus Corato-Zanarella, and Michal Lipson. Methods to achieve ultra-high quality factor silicon nitride resonators. *APL Photonics*, 6(7):071101, 07 2021. ISSN 2378-0967. doi:10.1063/5.0057881. URL `https://doi.org/10.1063/5.0057881`.

[8] T. M. Fortier, M. S. Kirchner, F. Quinlan, J. Taylor, J. C. Bergquist, T. Rosenband, N. Lemke, A. Ludlow, Y. Jiang, C. W. Oates, and S. A. Diddams. Generation of ultrastable microwaves via optical frequency division. *Nature Photonics*, 5:425–429, 2011. doi:10.1038/nphoton.2011.121.

[9] P. Del'Haye, A. Schliesser, O. Arcizet, T. Wilken, R. Holzwarth, and T. J. Kippenberg. Optical frequency comb generation from a monolithic microresonator. *Nature*, 450:1214–1217, 2007. doi:10.1038/nature06401.

[10] T. M. Fortier and E. Baumann. 20 years of developments in optical frequency comb technology. *Communications Physics*, 2:153, 2019. doi:10.1038/s42005-019-0249-y.

[11] T. J. Kippenberg, R. Holzwarth, and S. A. Diddams. Microresonator-

based optical frequency combs. *Science*, 332(6029):555–559, 2011. doi:10.1126/science.1193968.

[12] S. A. Diddams, D. J. Jones, J. Ye, S. T. Cundiff, J. L. Hall, J. K. Ranka, R. S. Windeler, R. Holzwarth, T. Udem, and T. W. Hänsch. Direct link between microwave and optical frequencies with a 300 THz femtosecond laser comb. *Physical Review Letters*, 84(22):5102–5105, 2001. doi:10.1103/PhysRevLett.84.5102.

[13] A. L. Gaeta, M. Lipson, and T. J. Kippenberg. Photonic-chip-based frequency combs. *Nature Photonics*, 13:158–169, 2019. doi:10.1038/s41566-019-0358-x.

[14] E. Lucas, P. Brochard, R. Bouchand, S. Schilt, T. Südmeyer, and T. J. Kippenberg. Ultralow-noise photonic microwave synthesis using a soliton microcomb-based transfer oscillator. *Nature Communications*, 11:374, 2020. doi:10.1038/s41467-019-14059-4.

[15] M. H. P. Pfeiffer, A. Kordts, V. Brasch, M. Zervas, M. Geiselmann, J. D. Jost, and T. J. Kippenberg. Photonic Damascene process for integrated high-Q microresonator based nonlinear photonics. *Optica*, 3(1):20–25, 2016. doi:10.1364/OPTICA.3.000020.

[16] T. Udem, R. Holzwarth, and T. W. Hänsch. Optical frequency metrology. *Nature*, 416:233–237, 2002. doi:10.1038/416233a.

[17] L. A. Lugiato and R. Lefever. Spatial dissipative structures in passive optical systems. *Physical Review Letters*, 58(21):2209–2211, 1987. doi:10.1103/PhysRevLett.58.2209.

[18] Y. K. Chembo and C. R. Menyuk. Spatiotemporal Lugiato-Lefever formalism for Kerr-comb generation in whispering-gallery-mode resonators. *Physical Review A*, 87(5):053852, 2013. doi:10.1103/PhysRevA.87.053852.

[19] T. Herr, V. Brasch, J. D. Jost, C. Y. Wang, R. Holzwarth, M. L. Gorodetsky, and T. J. Kippenberg. Temporal solitons in optical microresonators. *Nature Photonics*, 8:145–152, 2014. doi:10.1038/nphoton.2013.343.

[20] H. A. Haus and W. Huang. Coupled-mode theory. *Proceedings of the IEEE*, 79 (10):1505–1518, 1991. doi:10.1109/5.104225.

[21] J. Rutman. Characterization of phase and frequency instabilities in precision frequency sources: Fifteen years of progress. *Proceedings of the IEEE*, 66(9): 1048–1075, 1978. doi:10.1109/PROC.1978.11080.

[22] G. Huang, E. Lucas, J. Liu, A. S. Raja, S. Bhave, T. J. Kippenberg, and P. Del'Haye. Thermorefractive noise in silicon-nitride microresonators. *Physical Review A*, 99(6):061801(R), 2019. doi:10.1103/PhysRevA.99.061801.

[23] A. Arbabi and L. L. Goddard. Measurements of the refractive indices and thermo-optic coefficients of $Si_3N_4$ and $SiO_x$ using microring resonances. *Optics Letters*, 38(19):3878–3881, 2013. doi:10.1364/OL.38.003878.

[24] A. B. Matsko, A. A. Savchenkov, N. Yu, and L. Maleki. Whispering-gallery-

mode resonators as frequency references. II. stabilization. *Journal of the Optical Society of America B*, 24(6):1324–1335, 2007. doi:10.1364/JOSAB.24.001324.

[25] J. P. Gordon and H. A. Haus. Random walk of coherently excited solitons in optical fiber transmission. *Optics Letters*, 11(10):665–667, 1986. doi:10.1364/OL.11.000665.

[26] A. B. Matsko, A. A. Savchenkov, D. Strekalov, V. S. Ilchenko, and L. Maleki. Optical hyperparametric oscillations in a whispering-gallery-mode resonator: Threshold and phase diffusion. *Physical Review A*, 67(1):013814, 2003. doi:10.1103/PhysRevA.71.033804.

[27] Andrey B. Matsko and Lute Maleki. On timing jitter of mode locked kerr frequency combs. *Opt. Express*, 21(23):28862–28876, Nov 2013. doi:10.1364/OE.21.028862.

[28] D. T. Spencer, T. Drake, T. C. Briles, J. Stone, L. C. Sinclair, C. Fredrick, Q. Li, D. Westly, B. R. Ilic, A. Bluestone, N. Bhave, M. H. P. Pfeiffer, T. Weng, L. Yang, N. R. Newbury, T. J. Kippenberg, S. A. Diddams, and S. B. Papp. An optical-frequency synthesizer using integrated photonics. *Nature*, 557:81–85, 2018. doi:10.1038/s41586-018-0065-7.

[29] Zhixin Liu and Radan Slavík. Optical injection locking: From principle to applications. *Journal of Lightwave Technology*, 38(1):43–59, 2020. doi:10.1109/JLT.2019.2945718.

[30] R. Adler. A study of locking phenomena in oscillators. *Proceedings of the IRE*, 34(6):351–357, 1946. doi:10.1109/JRPROC.1946.229930.

[31] Erwin K. Lau, Liang Jie Wong, and Ming C. Wu. Enhanced modulation characteristics of optical injection-locked lasers: A tutorial. *IEEE Journal of Selected Topics in Quantum Electronics*, 15(3):618–633, 2009. doi:10.1109/JSTQE.2009.2014779.

[32] B. Razavi. *RF Microelectronics*. Prentice Hall, 2 edition, 2011. ISBN 978-0-13-713473-1.

[33] Kevin Scott and Michel Azarian. Phase noise of integer-n and fractional-n pll synthesizers. *Analog Devices Technical Article*, 2015. URL `https://www.analog.com/en/resources/technical-articles/phase-noise-of-integer-n-and-fractional-n-pll-synthesizers.html`.

[34] Bruce Griffiths. Phase noise theory: Ideal frequency multipliers and dividers. `https://www.ko4bb.com/~bruce/IdealFreqMultDiv.html`, 2024.

[35] X. et al. Xue. Mode-locked dark pulse kerr combs in normal-dispersion microresonators. *Nature Photonics*, 2015. URL `https://doi.org/10.1038/nphoton.2015.137`.

[36] A. B. Matsko and L. Maleki. On timing jitter of mode locked kerr frequency combs. *Optics Express*, 21(23):28862–28876, 2013. URL `https://doi.org/10.1364/OE.21.028862`.

[37] S. B. Papp, P. Del'Haye, and S. A. Diddams. Mechanical control of a microrod-resonator optical frequency comb. *Physical Review X*, 3(3):031003, 2013. URL `https://doi.org/10.1103/PhysRevX.3.031003`.

[38] A. Pasquazi et al. Micro-combs: A novel generation of optical sources. *Physics Reports*, 729:1–81, 2018. URL `https://doi.org/10.1016/j.physrep.2017.08.004`.

[39] K. J. Williams, D. A. Tulchinsky, J. C. Campbell, and S. Kar. High-power photodiodes for microwave photonics. *IEEE Journal of Quantum Electronics*, 52(1):0600712, 2016. doi:10.1109/JQE.2015.2504506.

# A

# Appendix 1

## A.1 Additional measurement data

This appendix presents supplementary measurement data that supports the results discussed in Chapter 4.

### A.1.1 50 GHz photodetector handling

The 50 GHz PD (XPDV2120R series, Coherent) is susceptible to permanent damage from reverse-biasing the PD when optical power is coupled to the PD without the PD being DC biased suitably [39] and requires a strict power-on and power-off sequence. The DC bias voltage (3.3 V nominal) must be applied and confirmed stable *before* optical power is introduced; optical power must be removed *before* the bias supply is switched off. Reversing this order causes permanent damage to the PD.
The DC responsivity was measured by recording the voltage developed across a 50 Ω termination at the RF output as a function of incident optical power, swept from −22 dBm to 10 dBm, to verify linearity and estimate the RF carrier power available at the analyser input. The measured responsivity is reported in Section A.1.2. The optical input was never permitted to exceed 10 dBm in any experiment, ensuring linear operation throughout. The maximum optical power that can be coupled to the PD is 16 dBm beyond which it will be permanently damaged. So a safety margin of 3 dB was taken into consideration so that a maximum optical power of 13 dBm was considered the upper limit for safe operation of the PD.

### A.1.2 DC responsivity of the 50 GHz photodetector

The DC responsivity of the 50 GHz PD was measured prior to phase noise characterisation to estimate the expected RF carrier power available at the analyser input.
As shown in Table A.1, the detector response remains approximately linear across the tested range, with an average responsivity of 0.34 A/W. This is lower than the datasheet minimum value of 0.5 A/W, attributed primarily to fibre-to-chip coupling loss at the detector input facet. The consequence is an RF carrier approximately 6 dB weaker than ideal, which shifts the measurement into the instrument-noise-limited regime at lower offset frequencies than would otherwise be expected. The optical power input to the photodiode never exceeded 10.5 dBm in any experiment, ensuring linear operation throughout.

**Table A.1:** Measured DC responsivity of the 50 GHz photodetector at $V_{\mathrm{bias}} = 3.3\,\mathrm{V}$.

| $P_{\mathrm{opt}}$ (dBm) | $P_{\mathrm{opt}}$ (mW) | $V_{\mathrm{DC}}$ (mV) | $\mathcal{R}$ (A/W) |
|---:|---:|---:|---:|
| −22 | 0.0063 | 0.10 | 0.317 |
| −15 | 0.0316 | 0.50 | 0.316 |
| −10 | 0.100 | 1.70 | 0.340 |
| −5 | 0.316 | 5.40 | 0.342 |
| 0 | 1.000 | 17.2 | 0.344 |
| +5 | 3.162 | 54.4 | 0.344 |
| +10 | 10.00 | 168.1 | 0.336 |

**DEPARTMENT OF ELECTRICAL ENGINEERING**
**CHALMERS UNIVERSITY OF TECHNOLOGY**
Gothenburg, Sweden
www.chalmers.se

CHALMERS
UNIVERSITY OF TECHNOLOGY